2013-12-17

A Kinetic Study of Aqueous Calcium Carbonate

Derek Daniel Harris
Brigham Young University - Provo

BYU ScholarsArchive Citation

Harris, Derek Daniel, "A Kinetic Study of Aqueous Calcium Carbonate" (2013). *Theses and Dissertations*. 3845.
https://scholarsarchive.byu.edu/etd/3845

A Kinetic Study of Aqueous Calcium Carbonate

Derek D. Harris

A thesis submitted to the faculty of
Brigham Young University
in partial fulfillment of the requirements for the degree of

Master of Science

David O. Lignell, Chair
Thomas H. Fletcher
Morris D. Argyle

Department of Chemical Engineering

Brigham Young University

December 2013

ABSTRACT

A Kinetic Study of Aqueous Calcium Carbonate

Derek D. Harris
Department of Chemical Engineering
Master of Science

Amorphous calcium carbonate (ACC) precipitation is modeled using particle nucleation, growth, and aggregation. The particles are tracked in terms of their radial size and particle density using direct quadrature method of moments (DQMOM). Four separate nucleation models are implemented and are compared to experimental data. In discord with a recent study, it is shown that classical nucleation, coupled with equilibrium chemistry, is in good agreement with experimental data. Novel nucleation mechanisms are presented which fit the experimental data with slightly greater accuracy. Using equilibrium chemistry it is shown that the equilibrium value of ACC is $pK_{eq} = 7.74$ at 24 ^{o}C, which is a factor of two smaller than the originally published equilibrium constant. Additionally, legacy equilibrium chemistry expressions are shown to accurately capture the fraction of calcium carbonate ions formed into ACC nano-clusters.

The density, solubility, and water content of ACC are discussed in a brief review, finding that a wide variety of properties are reported in the literature. Based on literature findings, it is proposed that the broad variety of reported properties may be due to ACC having several unique thermodynamic states.

Compelling evidence is presented exposing errors made by experimentalists studying the calcium carbonate system. The errors correct for mistakes of experimental kinetic data of the chemical-potential cascade of calcium carbonate due to the formation of meta-stable phases. Correlations are presented which correct for these mistakes.

A time-scale analysis shows the overlapping of kinetic scales and mixing scales within the calcium carbonate system. The kinetic scales are based on classical nucleation theory, coupled with diffusion limited growth. The mixing scales were computed using one-dimensional turbulence (ODT).

Keywords: DQMOM, calcium carbonate, ACC, particle-balance equation, chemical equilibrium, solubility product, calcite, vaterite, ODT

ACKNOWLEDGMENTS

I would like to thank the National Nuclear Security Administration for providing the funding used for the research presented in this thesis. Additionally, I would like to thank my wife for her support in my reasearch efforts.

TABLE OF CONTENTS

List of Tables

List of Figures

Chapter 1. Introduction

Calcium carbonate is a widespread, slightly soluble mineral that is widely used in industry and nature. In nature, calcium carbonate is used as a structurant in marine life, regulates the acidification of natural waters, and contributes to the natural removal of carbon dioxide from the atmosphere. In industry, calcium carbonate offers a pathway for effluent carbon dioxide sequestration and is used in the manufacturing of plastics, rubbers, paper, etc.

Due to the broad use of calcium carbonate in industry, advancing our understanding of this salt can increase industrial efficiency and productivity. In industry, stringent granular properties of calcium carbonate particles are often required such as particle size, habit, polymorph, and size variance. Calcium carbonate also hinders industrial efficiency by the scaling of processing equipment such as heat exchangers, reactors, and pipe networks. Both the scale inhibition and granular manipulation in industry would benefit from a greater fundamental understanding of aqueous calcium carbonate.

The aqueous calcium carbonate system has been studied extensively and yet much is still not known. Calcium carbonate formation has been shown to be dependent upon pH and ambient carbon dioxide. It is also known that the temperature of the calcium carbonate system strongly affects the crystal structure, or polymorph, of calcium carbonate formed. However, the mechanisms favoring the formation of one polymorph over another, known as polymorphic selectivity, remain unknown [3].

Calcium carbonate has five known structured polymorphs each with differing structural and thermodynamic properties. The anhydrous polymorphs are named, in order of increasing stability, vaterite, aragonite, and calcite. The hydrated polymorphs are called monohydrocalcite and ikaite. When these polymorphs precipitate from solution often the less stable polymorphs precipitate first as metastable intermediates. Solid calcium carbonate also forms amorphously, which is often the first phase formed in precipitation processes.

The calcium carbonate system is known to precipitate metastable polymorphs and phases as a precursors to more stable polymorphs [2]. This phenomenon occurs for many crystal systems and is called Ostwald's ripening or Ostwald's rule of stages. It is generally accepted that the calcium carbonate system undergoes a multi-phase dissolution and re-precipitation process which results in an intermittent cascade in the solute chemical-potential known as Ostwald's ripening. The mechanism for amorphous calcium carbonate (ACC) transformation and its role in Ostwald's ripening is a topic of uncertainty in the scientific literature.

In the last 5 years, ACC has been studied heavily due to research showing it behaves contrary to classical theories [1]. ACC is of prime importance due to it being the first solid-phase in the chemical potential cascade, which strongly influences the consequent crystalline polymorphs [1]. Amid several ACC studies, it is not clear whether ACC transformation to crystalline polymorphs is governed by the kinetics of the system or the thermodynamic state of the system [1].

Due to the multi-phase complexity of the calcium carbonate, very few studies have made attempts to kinetically model calcium carbonate precipitation. More simple aqueous salts have been kinetically modeled, for example the barium sulfate system. The barium sulfate system is perhaps the most studied and modeled crystallization system due to its simple nature of only having a single solid phase, or one polymorph. Barium sulfate also very similar to calcium carbonate. Both compounds are classified as slightly soluble salts and consist of divalent ion pairs. Classical nucleation theory has been applied to the barium sulfate system, hence it is a natural starting point to model calcium carbonate precipitation.

Classical nucleation theory predicts highly non-linear precipitation rates in terms of the chemical potential (thermodynamic driving force). This results in a broad range of time-scales, which in some cases overlap mixing scales. Despite this overlap, the spatial concentration gradients of precipitation systems are often ignored or dismissed in the scientific literature. Here, to account for mixing effects the one-dimensional-turbulence (ODT) model is employed because it resolves the mixing scales.

ODT is a powerful tool for turbulent reactive systems because of its low computational expense in which expensive chemical kinetics must operate on scalars throughout the domain. It is preferred to other turbulent models such as Reynold-averaged-Navier-Stokes (RANS) and large eddy simulation (LES) which model sub-grid fluctuations. The sub-grid mixing models used in these turbulence models often use the time mean spatially filtered values of reactive scalars in the non-linear rate expressions, which can be inaccurate. In this thesis, ODT is used to compute turbulent mixing scales which are then compared to the chemical kinetics of the system.

The primary objective of this work is to increase fundamental understanding of calcium carbonate precipitation. The bulk of this work operates on the assumption of the system being perfectly mixed, however the effects of turbulence are also considered in terms of a time scale analysis. Polymorphic selectivity is studied over different temperatures and compositions, under the assumption that the system is kinetically controlled. Various theoretical models are applied to the system of interest including nucleation, growth, aggregation, chemical speciation, and ionic-solution thermodynamics. The models are then compared to kinetic data in the literature.

In the remainder of this chapter recent literature findings of ACC physical properties will be presented due to their importance in solid-phase kinetic models. Popular and well cited scientific works are also discussed and critiqued.

1.1 Physical Properties of ACC

ACC precipitation occurs at high supersaturation ratios and in precipitation processes is favored over its more stable anhydrous cousins. The properties of the anhydrous polymorphs are well established, and are reproduced routinely in experiments [2, 4, 5]. However, there are several inconsistencies in the literature pertaining to the physical properties of ACC, such as its density, solubility and water content [4, 6–10].

The literature reports a wide range of solubilities for ACC, shown in Figure 1.1. Clarkson et al. [11] as well as Brecevic and Nielsen [8] developed differing correlations for the solubility of hydrated ACC, which vary by about 40% of each other as shown in Figure 1.1. Brecevic and Nielsen [8] determined the temperature-dependent equilibria by slowly diluting a supersaturated solution with ACC until the ACC dissolved. Clarkson et al. [11] combined solutions of Na_2CO_3 and $CaCl_2$ together and noted that at pseudo-steady state the liquid chemistry was metastable and indicated a near equilibrium point. They then verified this by adding ACC to solution, reaching the same ion activity product (IAP) of calcium and carbonate ions due to dissolution. The IAP in this work is defined as the product of the activity of calcium ions and carbonate ions. The IAP is the driving force for nucleation processes which is shown to be true in chapter 3.

Also shown in Figure 1.1 are equilibrium values from experiments conducted by Ogino et al. [2]. They observed a steady-state value of the IAP when mixing solutions of Na_2CO_3 and $CaCl_2$, inferring a near equilibrium value. The values presented are adjusted in accordance with the model presented in Ref. [2], as there is a disparity between their presented model and their data. This is discussed further in Section 1.4. More recently, ACC formed in studies presented in Refs. [1, 12] was reported to have a solubility product one order of magnitude lower than that presented in Refs. [8, 11]. The formation of this ACC is discussed in detail in Section 1.2.

The wide variability of ACC solubility may be attributed to the large number of ACC variations emerging in the scientific literature. ACC has been investigated in terms of four different discrete forms: highly-disorded hydrated, disordered hydrated, anhydrous, and biogenic anhydrous [6]. Additionally, a review investigating the question, “how many amorphous calcium carbonates are there?” was conducted by Cartwright et al. [7]. Their findings classify ACC into several categories. Additive-free synthetic ACC varieties are

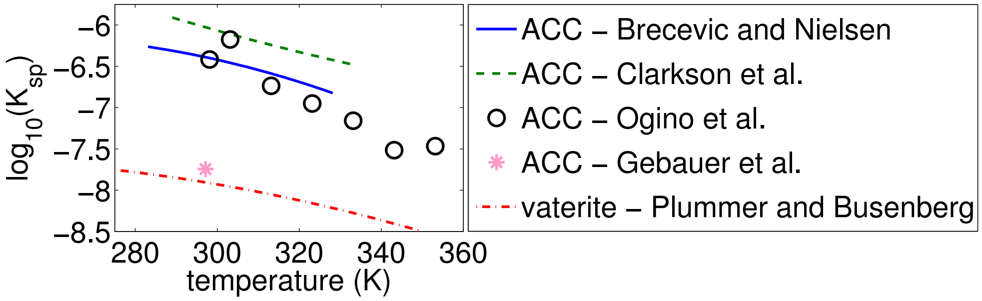

Figure 1.1: Wide disparity in the solubility product of ACC measured by Gebauer et al. [1] and other experimentalists [2, 8, 11]. Vaterite solubility is included for reference. Solid line - [8], Dashed line - Clarkson et al. [11], circles - Ogino et al. [2], asterisk - Gebauer et al. [1], dash dot line - Plummer and Busenberg [4].

classified as: unstructured ACC [2,8,9,11,13–16], liquid ACC [17], proto-vaterite, and proto-calcite [1,18,19]. Cartwright et al. also categorized several biogenic variations of ACC and a polymer induced synthetic ACC [7]. Others have stated that due to the variation of solubility of ACC it cannot be characterized as a thermodynamic phase [20].

A less likely cause of variability in the reported solubility of ACC is that two hydrated forms of calcium carbonate have solubility products in the same regime as ACC. The known hydrated forms of ACC are called ikaite and monohydrocalcite, and are usually formed in specific environmental conditions. An ionic molar ratio of [5Ca : 1Mg] is key for creating favorable precipitation conditions for monohydrocalcite [5, 21, 22]. Similarly, ikaite is favored at specific conditions, including low temperatures, high pressures, and high pH [11, 23].

The scientific literature also reports variability in ACC density and water content. Faatz et al. [24] studied the mechanical properties of hydrated ACC and found that it had a specific gravity of 1.90. Others observe hydrated ACC to have a specific gravity of 1.62, but when precipitated in the presence of a block-copolymer additive, a value of 1.9 was found [9, 10]. Molecular-dynamics simulations found ACC density to be much higher, as high as 2.71 g / cm^3 [25]. The water content of ACC was found to be $CaCO_3 \cdot 0.5H_2O$ by Faatz et al. [24]. Others report water content of ACC to be $CaCO_3 \cdot 1.0H_2O$ [8]. Additional sources have found the water content to range from zero, to at least 1.38 water molecules per monomer unit [14, 25, 26].

At high supersaturations, the calcium carbonate system is complex, offering several kinetic pathways to solid-phase calcium carbonate. There are several amorphous phases and hydrated polymorphs that exhibit solubilities larger than that of vaterite. Amid these observations, a single property, such as density, solubility, or water content, is not informative enough to properly characterize this amorphous material. In some cases ACC is synthesized without reporting any of its physical properties, creating uncertainty as to which variety of ACC was produced.

There exists extensive uncertainty in the physical and thermodynamic properties of ACC, which makes applying a theoretical kinetic model challenging. Classical-nucleation theory relies heavily on the molar volume of a given solid [27]. Theoretical approaches for deriving surface energies of the nucleation crystals are dependent upon the solid-phase density and water content [28]. Nucleation kinetic theory is also very sensitive to the equilibrium state of the precipitating solute, as supersaturation is defined in reference to that state.

For the kinetic study in this work, it is assumed that ACC is anhydrous and has a specific gravity of 1.9. The concentration-activity based solubility constant is assumed to equal to 1.8E-8 for simulations reproducing data from Gebauer et al. [1] otherwise expressions from Brecevic and Nielsen [8] are used. ACC is also assumed to be anhydrous.

1.2 Gebauer's Experiment

Among recent ACC publications in the scientific community, few had as much of an impact as Gebauer et al. [1], who discovered *stable* ACC nano-particles in solution. Their work called for molecular simulations of the system to advance the understanding of stable ACC.

They conducted an experiment using solutions of aqueous calcium chloride and sodium carbonate. The former was slowly added to a bulk solution of the latter, increasing the su-

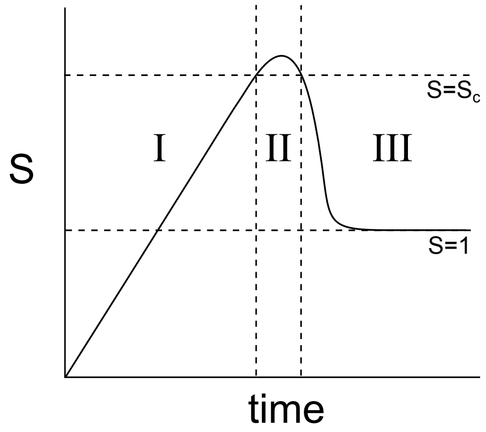

Figure 1.2: Typical LaMer diagram, showing the three experimental stages observed in the experiment by Gebauer et al. [1]; Stage I - prenucleation stage, Stage II - nucleation event, and Stage III - pseudo-steady-state-growth stage. S is the supersaturation ratio, and S_c is the critical supersaturation ratio.

persaturation ratio of calcium carbonate until it surpassed some critical point, S_c. After exceeding the critical supersaturation ratio, calcium carbonate precipitated and the calcium concentration quickly dropped to an equilibrium value generating a curve commonly referred to as a LaMer diagram [29] (see Figure 1.2).

Gebauer et al. [1] report three distinct stages in the calcium trace over the course of each experiment. These stages are identified here as the prenucleation stage, the nucleation event, and the post nucleation or pseudo-steady-state-growth stage (stages I, II, and III, respectively, see Figure 1.2). It was found that as calcium was slowly added to the carbonate solution, a disparity existed between the calcium added and the calcium detected during the prenucleation stage, an indication of bound-calcium ions. This phenomenon occurs below the supersaturation of the observed precipitant indicating stable ACC. Particles two nanometers in diameter were observed prior to the nucleation event. These observed phenomena made a big impact in the scientific community and created the hypothesis that bound-calcium is stable as a prenucleation cluster, contrary to classical-nucleation theory.

The experiment consisted of a solution with an initial volume of 25 mL of 10.0 mM Na_2CO_3 (aq). The pH of the initial solution was adjusted to different values and held constant for a parametric study of five different pH values ranging from 9.0 to 10.0. A solution of 10 mM CaCl (aq) was added to the carbonate solution at a rate of 10 μL/min. The pH of the solution was kept constant by the addition of 10 mM NaOH, whose flow rate was regulated by a computer-controlled titration. The concentration of free-calcium ions present in solution was monitored by a calcium-selective probe. The calcium-selective probe was re-calibrated for each of the five pH experiments. All experiments operated at 24 ^{o}C exposed to the atmosphere. The in-diffusion of carbon dioxide was thought to create less than 4% error in amount of calcium ions in solution.

Gebauer et al. [1] observed the formation of two variants of ACC, named proto-vaterite and proto-calcite. When proto-calcite formed, calcite was observed shortly after, and similarly, vaterite was formed shortly after proto-vaterite precipitation. Wide angle x-ray scattering (WAXS) was used to identify the crystal polymorphic structure 180 to 600 minutes after nucleation of these amorphous phases.

1.3 Critique of Gebauer et al.

Since only one temporal sample was taken per pH experiment, and due to the long residence time of the calcium carbonate solutions, it is suggested that metastable vaterite may have formed without observation due to re-precipitating of vaterite into calcite, as has been reported in other studies [2, 11, 30, 31]. The time-scales for vaterite-to-calcite transformation range from 100 to 1000 minutes at 25 ^{o}C making it possible for vaterite to exist as an unobserved intermediate. This is increasingly likely when a study shows that at high pH values the transformation of vaterite to calcite is strongly retarded at a pH of 10.0 [32]. Hence, the polymorphic transition occurs rapidly at low pH values, and slowly at high pH values.

Gebauer et al. [1] made the assumption that the activity of ions in solution behaved ideally since the ionic strength, I, remained slightly less than 0.1. The ionic strength is defined as,

$$I = \frac{1}{2} \sum_{i=1}^{n} z_i^2 C_i \tag{1.1}$$

where C_i is the concentration of an ion of species i, and z_i is its corresponding charge. The ionic strength is important because as the ionic strength increases, short term ionic interactions become more and more important. The Davies model does not theoretically take into account short term ion interactions, and hence is only sufficient up to an ionic strength of $I = 0.1$. In Ref. [1] the ions were assumed to behave ideally. Using the Davies equation, which is accurate up to ionic strengths of approximately 0.1 [33], the activity coefficient, γ, of divalent ions is 0.58 at a pH of 10.0. The calibration solution used by Gebauer et al. [1] was a solution of calcium chloride and the divalent-activity coefficients for which are much higher, about 0.9 or more. Consequently, the disparity in activity coefficients creates error of up to 50%, based on the ratio of the disparate activity coefficients.

Gebauer et al. [18] also states that Debye-Huckle activity models erroneously correct chemical potential by ignoring formation of stable calcium carbonate in these systems [12]. This critique is somewhat in accordance with dated studies which discuss the weaknesses and limitations of Debye-Huckel thermodynamics [34–36]. However, as is shown in Section 4.1, the Davies equation, an extension of Debye-Huckel theory, used in combination with key chemical species predicts bound calcium behavior shown by Gebauer et al. [1]. Additionally, the equilibrium constant for bound calcium, $CaCO_3^o$, was developed without the use of a calcium-specific probe [4]. Since bound calcium data from two different experiments are reproduced using a single model (developed in this thesis), credibility is added to both the activity model and the equilibrium constant describing bound calcium. This is even more significant considering that the experiments used different sensory methods to measure bound-calcium ions.

1.4 Ogino's Experiment

Ogino et al. [2] published work studying calcium carbonate polymorphic selectivity and showed the kinetic time-scales of polymorphic transformation at moderate supersaturation ratios. The emphasis of their work was to study how temperature affects the polymorphic preference of the calcium carbonate system. While several works in the literature study polymorphic selectivity, few offer the polymorphic kinetic data that Ogino et al. provides, making their work ideal for kinetic analysis.

Ogino et al. [2] precipitated calcium carbonate by quickly mixing solutions of sodium carbonate and calcium chloride. The polymorph precipitated was highly dependent upon the temperature, and also the initial concentration of the reagent solutions. Ogino et al. showed that aragonite formed at higher temperatures at a fast rate and calcite was favored at low temperatures at a slow rate. Vaterite was favored at intermediate temperatures at an intermediate rate. ACC was a precursor to all polymorphs at all temperatures investigated.

Ogino et al. [2] computed the ion activity product (IAP) as a function of time using a BASIC computer program combined with a temporal signal from a pH probe. The BASIC code was based on a chemistry model developed by Plummer and Busenberg [4]. When re-implementing the computer model coded by Ogino et al. [2] the simulated results do not match their published theoretical values. This suggests that a mistake may have been incorporated into the BASIC equilibrium chemistry algorithm.

A short case study was conducted to understand why the data and the model presented by Ogino et al. [2] were different. Through stringent investigation of the chemistry model the error in the BASIC code used by Ogino et al. was reproduced. The second plot in Figure 1.3 shows that the re-implemented Plummer and Busenberg [4] model is consistent with the data reported by Ogino et al. when a sign error was imposed into the code. This same plot shows that the BASIC model fails to match data by other experimentalists [1]. The supposed sign error would also correspond to reversing the reaction direction forming the calcium carbonate complex, $CaCO_3^o$.

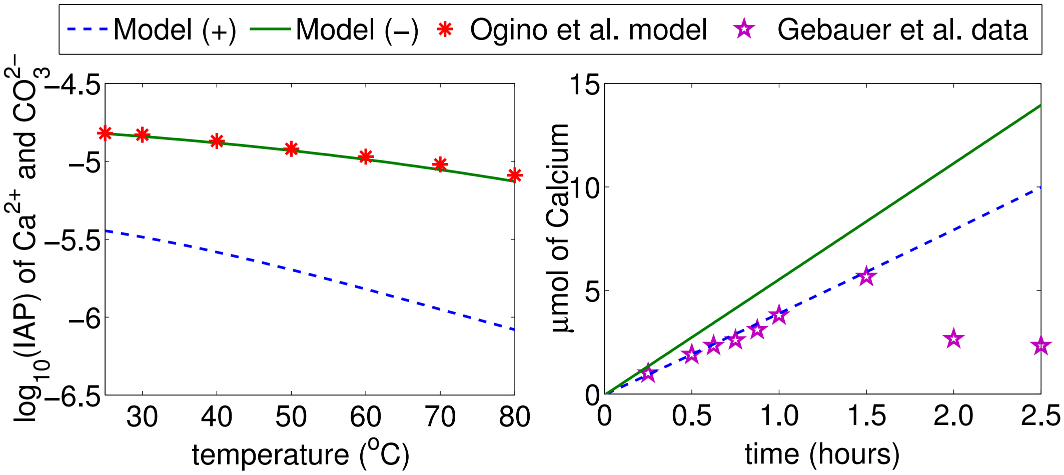

Figure 1.3: Left plot: Compares three models over a the temperature range of 25 to 80 ^{o}C. Right plot: comparison between two chemistry models and data from a precipitation experiment conducted by Gebauer et al. at 25 ^{o}C. Dashed line: predicted IAP or calcium concentration using the model developed by Plummer and Busenberg [4]. Solid-line: predicted IAP or calcium concentration using the model developed by Plummer and Busenberg [4] while introducing a sign error. Asterisk: predicted IAP using the model Ogino et al. [2] coded in BASIC. Star: measured calcium concentration by Gebauer et al.

If the data set published by Ogino et al. is indeed inaccurate it makes quantitative comparisons with the experimental observations challenging. To estimate the correct IAP of calcium and carbonate ions the two chemistry models were used to create a parametric table in terms of the extent of precipitation. A correlation relating their apparent model to the model defined by Plummer and Busenberg is given by Equations 1.2 and 1.3). These correlations correspond to the 25 ^{o}C and 50 ^{o}C experiments, respectively

$$\begin{aligned}\ln\left(IAP^{25C}_{correct}\right) = & -0.0032450 \cdot \ln(IAP_{Og})^3 - 0.14768 \cdot \ln(IAP_{Og})^2 \\ & - 1.3378 \cdot \ln(IAP_{Og}) - 13.632, \end{aligned} \tag{1.2}$$

and

$$\begin{aligned}\ln\left(IAP^{50C}_{correct}\right) = & -0.0020413 \cdot \ln(IAP_{Og})^3 - 0.096372 \cdot \ln(IAP_{Og})^2 \\ & - 0.66910 \cdot \ln(IAP_{Og}) - 11.274. \end{aligned} \tag{1.3}$$

Implied meta-stable equilibrium points are reported by Ogino et al., namely ACC equilibrium. Figure 1.1 shows the adjusted values of Ogino et al. equilibrium. In general, the adjusted values are nearly one order of magnitude lower than that reported by Ogino et al.

Once the aqueous data are corrected, the data are more consistent with other solubility data within the literature. This means that the application of a solid phase model will match the data more accurately. Due to this correction, the data found by Ogino et al. [2] can be reproduced using precipitation theory, developed here, albeit only over a narrow range of conditions, shown in Appendix A.

1.5 Thesis Objectives

The objective of this thesis is to advance our fundamental understanding of calcium carbonate precipitation by accomplishing the following:

- Develop theoretical kinetic models for ACC precipitation. The models will use assumptions based on findings from the scientific literature. The basis for this model is presented in Chapters 2 and 3.
- Compare the kinetic models to experimental data as well as models employing classical nucleation frameworks. This is shown in Chapter 4.
- As described earlier this chapter, ACC has a wide range of reported equilibrium values. The equilibrium point of ACC will also be studied making use of the kinetic models. This is shown in Chapter 4.
- Conduct a time scale analysis for a theoretical kinetic model describing the concurrent precipitation of ACC, vaterite, aragonite, and calcite. This is shown in Chapter 5. This will show the importance of accounting for mixing in calcium carbonate precipitation.

Chapter 2. Methods

Several numerical methods are discussed in this chapter. Those discussed are quadrature method of moments, direct quadrature method of moments and the one-dimensional turbulence (ODT) formulation.

2.1 Quadrature Method of Moments

Quadrature method of moments (QMOM) is a technique for tracking Eulerian particles in a system. QMOM evolves the particle-size distribution in a mathematically elegant way which saves on the computational expense by reducing the number of scalars that are transported. The term “quadrature“ can be described as simple numerical integration, hence the analytical computation of the radial moments are approximated via numerical integration. Note that while radial moments are used here, moments can be parameterized in terms of any internal coordinate, such as log-radius, mass, Gibbs energy, etc. Also note, that multi-variant distributions can also be transported using similar methods [37].

The moments of the distribution are defined as

$$M_k = \int_0^\infty \eta(r) r^k dr. \tag{2.1}$$

Here, M_k is the k^{th} moment of interest, r is the internal coordinate (particle radius), and $\eta(r)$ is the particle-size distribution. The use of moments reduces the computational expense of temporally evolving the entire particle-size distribution. Moments can be used to approximate the original particle-size distribution using various closure methods [38]. Here, closure using quadrature is discussed in detail.

Equation 2.1 requires closure in most cases, which can be done using quadrature. Quadrature is the means of closure of the unknown particle-size distribution η. Closure is achieved using weights and abscissa computed from the moments using the product-difference algorithm [39]. Equation 2.2 shows the quadrature equivalent of Equation 2.1,

$$M_k = \sum_{i=1}^{n} w_i r_i^k. \tag{2.2}$$

Here, n is half the number of moments transported, w_i is a weight of the particle-size distribution and r_i is the corresponding abscissa (or independent variable) of weight w_i. The weights and abscissa are computed from the moments using the product-difference algorithm [39]. The units between Equations 2.1 and 2.2 are consistent, hence the weights have the same units as $\eta(r)\Delta r$. These moment definitions will be used in the derivation of QMOM which follows.

Conceptually, moment methods are analogous to tracking discretized versions of the particle size distribution. Figure 2.1 shows how the particle size distribution is represented using quadrature. The first plot shows a typical particle size distribution of a particle population. This distribution can be transformed into moments using Equation 2.1. The weights of the distribution, shown in the second plot, can then be recovered using quadrature [39].

The derivation of moment evolution equation is presented here in terms of radial moments, starting with the particle balance equation,

$$\frac{\partial \eta(r)}{\partial t} + \frac{\partial(\eta(r)G(r))}{\partial r} = B - D. \tag{2.3}$$

Here, η is the particle density function, $G(r)$ is the rate of growth, and r is the independent variable, internal coordinate, and particle radius. The variables B and D refer to birth and death, respectively, and are computed using nucleation, breakage, and aggregation. These processes are discussed in detail in Chapter 3.

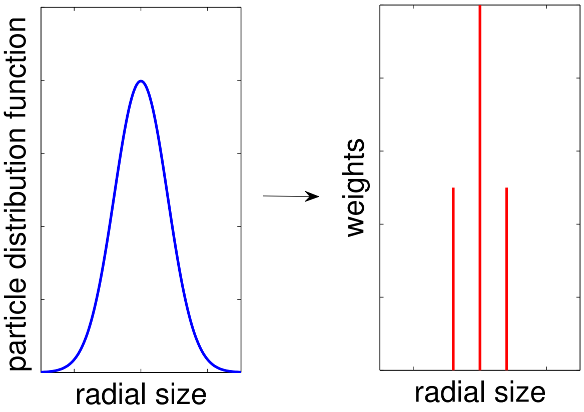

Figure 2.1: Conceptual illustration of how the particle size distribution is tracked using moment methods. Left plot: shows a particle size distribution. Right plot: shows a six-moment representation of the distribution in the first plot using quadrature.

The first operation needed for the transformation of the particle balance equation (PBE) into a moment equation is to multiply both sides of the equation by $r^k\partial r$. Next, both sides are integrated over the entire radial domain, in this case from zero to infinity, shown by equation

$$\int_0^\infty \frac{\partial \eta(r)}{\partial t} r^k \partial r + \int_0^\infty \frac{\partial(\eta(r)G(r))}{\partial r} r^k \partial r = \int_0^\infty (B - D) r^k \partial r. \tag{2.4}$$

The integral operation commutes with the derivative, hence changing the order of the operations is done for the first term in Equation 2.4.

$$\frac{\partial(\int_0^\infty \eta(r) r^k \partial r)}{\partial t} + \int_0^\infty \frac{\partial(\eta(r)G(r))}{\partial r} r^k \partial r = \int_0^\infty (B - D) r^k \partial r \tag{2.5}$$

Looking closely at the second term in Equation 2.5, integration by parts moves the r^k term into the derivative and generates an additional term.

$$\frac{\partial(\int_0^\infty \eta(r) r^k \partial r)}{\partial t} + \eta(r)G(r)r^k\Big|_0^\infty - k\int_0^\infty \eta(r)G(r) r^{k-1} \partial r = \int_0^\infty (B - D) r^k \partial r \tag{2.6}$$

Next, substitute the moment definition in Equation 2.1 into equation 2.6 and make the quadrature approximation given by Equation 2.2.

$$\frac{\partial M_k}{\partial t} + \eta(r)G(r)r^k\Big|_0^\infty - k\sum_{i=1}^{n} w_i G(r_i) r_i^{k-1} = \int_0^\infty (B-D)r^k \partial r \tag{2.7}$$

Note that all dependence upon the particle density function has been removed, with the exception of the second term. This term represents the flux of particles in and out of the domain at zero and infinity and is equal to zero for radial moments, which results in equation,

$$\frac{\partial M_k}{\partial t} = k\sum_{i=1}^{n} w_i G(r_i) r_i^{k-1} + \int_0^\infty (D-B)r^k \partial r. \tag{2.8}$$

Equation 2.8 shows the transport equation used by QMOM equation for radial moments and assumes no diffusion or convection out of the system.

2.2 Direct Quadrature Method of Moments

This section derives direct quadrature method of moments (DQMOM) from the QMOM derivation. Note that DQMOM is theoretically identical to QMOM but behaves differently numerically. DQMOM transports the weights and abscissas directly in place of the moments.

To convert the QMOM to DQMOM several algebraic transformations are needed. This can be done by substituting Equation 2.2 into Equation 2.8, followed by algebraic manipulation. Also, to decrease the length of the equations, the right hand side of Equation 2.8 shall be denoted as a source term S_k. These operations yield equation

$$\sum_{i=1}^{n} \frac{\partial (w_i r_i^k)}{\partial t} = S_k. \tag{2.9}$$

Then use the product rule to expand the first term on the left hand side, resulting in equation,

$$\sum_{i=1}^{n}\left(\frac{\partial w_i}{\partial t}r_i^k + w_i\frac{\partial r_i^k}{\partial t}\right) = S_k. \tag{2.10}$$

Next, use the chain rule to expand the derivative of the abscissa r_i, shown by

$$\sum_{i=1}^{n}\left(\frac{\partial w_i}{\partial t}r_i^k + k w_i r_i^{k-1}\frac{\partial r_i}{\partial t}\right) = S_k. \tag{2.11}$$

From this point, a linear system of $2n$ equations and $2n$ unknowns can be formulated to compute the terms $\frac{\partial w_i}{\partial t}$ and $\frac{\partial r_i}{\partial t}$. This can be illustrated using the classic matrix formulation **A*x=b**. The matrix, **A**, used in DQMOM is defined as,

$$\mathbf{A}_{1,k} = \left[r_1^k, r_2^k, ..., r_n^k, k w_1 r_1^{k-1}, k w_2 r_2^{k-1}, ..., k w_n r_n^{k-1}\right]. \tag{2.12}$$

The array **x** contains the unknown variables needed for DQMOM, and is

$$\mathbf{x} = \left[\frac{\partial w_1}{\partial t}, \frac{\partial w_2}{\partial t}, ... \frac{\partial w_n}{\partial t}, \frac{\partial r_1}{\partial t}, \frac{\partial r_2}{\partial t}, ..., \frac{\partial r_n}{\partial t}\right]. \tag{2.13}$$

Any combination of moment indices, k, can be used to create the system of linear equations. Here, a numerically sequential vector starting with zero and ending with n is used. The choice of the vector may be numerically important in reducing the condition number of the matrix **A**. A numerically sequential choice for the moment indices results in the source-term vector, **b**, being,

$$\mathbf{b} = \left[S_0, S_1, ..., S_n\right]. \tag{2.14}$$

Equations 2.12, 2.13, and 2.14 constitute the DQMOM formulation and can be used to evolve weights and abscissas in time. In the author's opinion, DQMOM is the preferred method over QMOM for the following reasons:

- DQMOM has a more intuitive meaning since weights reflect the state of the particle density function.
- DQMOM can be expanded upon to include multiple internal coordinates.
- DQMOM uses commonly used numerical methods, such as a matrix inversion rather than the product-difference algorithm.
- The minimum time step required in numerical methods is easier to compute.

QMOM also has benefits, for example, moments are more naturally transported in a CFD code, since all the moments are intensive quantities. In DQMOM, the abscissa are not intensive properties hence precaution should be taken when transporting in ODT.

Both DQMOM and QMOM become ill-conditioned as additional moments are added. The methods also mutually fail when abscissa overlap or when weights approach zero due to singularity (an infinite number of solutions). This can occur under several circumstances, when growth, aggregation, or nucleation processes predict mono-dispersed distributions, when the ordinary-differential-equation (ODE) solver takes too large of time steps, when systems with fast nucleation and slow growth are considered, etc. Typically both DQMOM and QMOM are limited to transporting 10 to 14 moments. Also, aqueous precipitation systems have very fast numerics at short times which require very small time steps when numerically evolving temporal profiles using explicit ODE solvers.

2.3 One-Dimensional Turbulence Model

One dimensional turbulence is a method for modeling turbulence of simple flows coupled with complex chemical kinetics [40]. Several turbulence models are able to accurately model simple flows, however these models all under-resolve fine mixing structures. This can lead to substantial error due to the strong non-linear characteristics of kinetic models. The strength in ODT is that the fine mixing structures are resolved due to the 1-D nature and relatively low computational cost of of the model.

ODT models a one-dimensional line-of-sight through a turbulent flow. The ODT model undergoes two concurrent processes: diffusive reactive transport equations and convective transport. Diffusion transport is achieved by solving one-dimensional transport equations while the convective transport is modeled by generating eddy events called *triplet maps* along the 1-D domain. The triplet maps are generated stochastically in combination with criteria based on the local shear on the line.

2.3.1 Diffusive Transport

The 1-D transport equations solved for on th ODT line is given by the generic partial differential equation

$$\frac{\partial y}{\partial t} = D_y \nabla \cdot j_y + S_y, \tag{2.15}$$

where y is any scalar, D_y is the scalar diffusion coefficient, j_y is the scalar flux, and S_y is the source term for the scalar y. The PDEs are solved using finite-volume methods. The boundary conditions are dependent upon the application.

2.3.2 Convective Transport

A diagram showing the affect of a triplet map on a scalar profile, $y(x)$, is shown in Figure 2.2. The solid line denotes an arbitrary scalar profile which undergoes a triplet map process at x_0, the diameter of the eddy event is denoted by l_e. After the triplet-map process occurs, the dashed line remains. The definition of the triplet map is mathematically given by the piecewise formulation,

$$Y(x) = \begin{cases} y(3x - 2x_0 + l_e) & -\frac{1}{2}l_e \leq x - x_0 < -\frac{1}{6}l_e \\ y(-3x + 4x_0) & -\frac{1}{6}l_e \leq x - x_0 < \frac{1}{6}l_e \\ y(3x - 2x_0 - l_e) & \frac{1}{6}l_e \leq x - x_0 < \frac{1}{2}l_e \end{cases} \tag{2.16}$$

Here, y represents the vector of any scalar on the ODT line which is undergoing the triplet-map process to form the new 1-D profile. The new ODT profile is represented by $Y(x)$

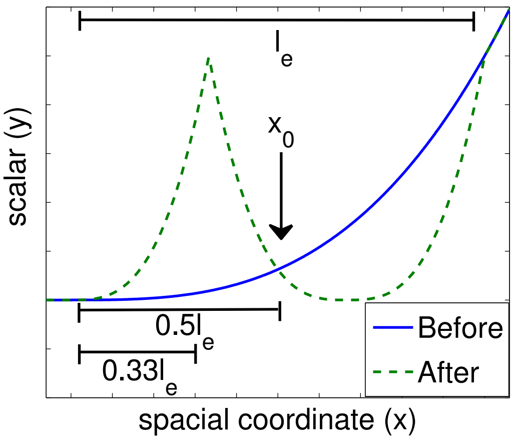

Figure 2.2: Plot showing ODT triplet-map process. Solid line: shows an arbitrary scalar profile, y, in space, x. Dashed line: shows the scalar profile after an instantaneous triplet-map process, where l_e is the eddy size and x_0 is the center of the eddy event.

and the center of the triplet map occurs at x_0. The variable, l_e, is the eddy size, and the independent spatial variable, x, is defined in terms of an arbitrary origin. Qualitatively, triplet maps defined by Equation 5.3 increase scalar gradients. The gradients are increased by duplicating the original profile three times, compressed by a factor of three, while inverting the central profile. This results in a continuous scalar profile, with increased gradients.

The use of triplet-maps has several limitations. They are instantaneous, so that eddies are unable to occur concurrently. This means that one eddy does not effect other eddies directly, albeit through the indirect means of increasing shear, which in turn, increases the consequent eddy probability.

The triplet map is the primary means by which turbulence is generated in the ODT model and the criteria for placing eddy locations and sizes are responsible for ODT's success in accurately simulating turbulence. Eddy events, or triplet maps, occur stochastically, however the selection process is not purely random. The probability of eddy occurrence is higher in regions where there is high fluid shear. For a comprehensive explanation on the eddy sampling process, see Ref. [41].

Chapter 3. Nucleation, Growth, and Aggregation

This chapter discusses several possible nucleation, growth, and aggregation mechanisms which operate within framework of QMOM and DQMOM. Heterogeneous nucleation, growth, and aggregation mechanisms are functions of the particle radius and fully employ the offered functionality of these methods.

In this chapter, four different homogeneous nucleation models are presented and developed. Each of them make different assumptions about the limiting processes governing nucleation. Two different growth models are presented and three different aggregation models, each with their respective assumptions. The aqueous chemistry model for this system is also discussed in this chapter. Heterogeneous nucleation is also discussed.

3.1 Classical Nucleation

Nucleation occurs when a new phase forms within a bulk phase and is a theoretical basis for predicting the rate of particle formation in vapors, liquids, and melts. Classical-nucleation theory (CNT) is a common approach to describing precipitation systems and was first applied to the water-vapor system. Due to its wide applicability, specialized variations of CNT are often used depending on the specific application.

Over a wide range of conditions, crystal systems have slow time-scales, despite a large driving force pushing for precipitation. CNT attributes this behavior to the unfavorable creation of an interface between the nucleate and the bulk phase. Once the nucleates are formed, precipitation occurs via growth which is kinetically limited.

CNT is the primary basis for describing nucleation rates for crystallization systems [27,42–44]. It was used to describe barium sulfate [27] as well as the polymorphic selectivity in the calcium carbonate systems [42].

CNT has two distinct types of nucleation, homogeneous and heterogeneous nucleation. Homogeneous nucleation occurs when the condensed phase is created in the bulk phase. Heterogeneous nucleation occurs when the condensed phase nucleate on foreign particulates which decrease the interfacial Gibbs energy between the bulk and condensed phase. In this work, homogeneous nucleation is assumed to be the dominant mechanism for nucleation, since experimental data available was collected using distilled water as the solvent. Heterogeneous nucleation is also discussed. Novel mechanisms for nucleation are also investigated.

3.1.1 Classical Homogeneous Nucleation Theory

The basic approach to CNT is to consider a prenucleation distribution which consists of clusters of monomer species, ω_i. These species interact and react with monomer units, ω_1, according to a series of reversible chemical reactions. The critical size, c, of these clusters corresponds to a monomer cluster reactant which reacts irreversibly. The irreversible equation is given as,

$$[\omega_{\mathrm{c}}] + [\omega_1] \xrightarrow{k_{f,c}} [\omega_{\mathrm{c}+1}]. \tag{3.1}$$

The reaction rate be computed using the critical forward-rate constant $k_{f,c}$, the monomer concentration $[\omega_1]$, and the concentration of critical nucleation embryos, $[\omega_c]$. The rate of reaction of the irreversible reaction, shown in equation 3.1 is equal to the nucleation rate. Hence, the nucleation rate, J_{nuc}, is simply computed

$$J_{nuc} = k_{f,c}[\omega_1][\omega_c]. \tag{3.2}$$

A key assumption of this approach is that prenucleation embryos can only increase in size by single monomer addition. Hence, monomer clusters of size i can only interact with the species ω_1. This is thought to be a good assumption because the prenucleation distribution decays exponentially.

To compute the concentration of the critical species, $[\omega_c]$, the equilibrium pre-embryo distribution is needed, which can be parameterized in terms of the net Gibbs energy change of the system due to formation of a single particle. Here, the derivation for energy barrier inhibiting nucleation is presented. Starting with the multi-phase Gibbsian, a differential change in the Gibbs energy of a system or control volume can be computed using equation,

$$dG_S = VdP - SdT + \sum_{i=1}^{n}\sum_{j=1}^{\xi}\mu_{i,j}dN_{i,j} + \sum_{\substack{j=1 \\ j\neq k}}^{\xi}\sum_{k=j}^{\xi}\sigma_{j,k}dA_{j,k}. \tag{3.3}$$

Here, G_S is the total Gibbs free energy of the multi-phase system, V is the molar volume of the system, P is the absolute pressure, S is the molar entropy, T is the absolute temperature, n is the total number of species i in the system, and ξ is the total number of phases. $\sigma_{j,k}$ is the interfacial tension between phases j and k and $A_{j,k}$ is the interfacial area between those two phases. $\mu_{i,j}$ is the chemical potential of species i, in phase j and N_i is the number of moles of chemical species i.

Using equation 3.3, consider a single-phase system where a second phase, j, is formed. Assume that the transformation occurs under isobaric and isothermal conditions. Integrating from the single-state phase to the dual-state results in equation,

$$\Delta G_{S,j} = \sum_{i=1}^{n}\mu_{i,b}\Delta N_i - \sum_{i=1}^{n}\mu_{i,j}\Delta N_i + \sigma_{bj}\Delta A_{bj}. \tag{3.4}$$

Here, $\Delta G_{S,j}$ is the Gibbs energy of the entire system due to the formation of the new phase, j. Also in Equation 3.3, $\mu_{i,b}$ and $\mu_{i,j}$ are the chemical potentials of species i in the bulk and condensed phases, respectively. σ_{bj} is interfacial energy between the bulk and condensed phase and like-wise A_{bj} is the interfacial area between the same phases. Equation 3.4 also assumes that the chemical potential of the bulk and liquid phases remains constant.

The species N_i can be written in terms of stoichiometric coefficients, z_i, and the number of monomer units, N_m, computed as

$$z_i = \frac{\Delta N_i}{\Delta N_m}. \tag{3.5}$$

Combining equations 3.5 and 3.4 gives,

$$\Delta G_{S,j} = \sum_{i=1}^{n} \mu_{i,b} \Delta N_m z_i - \sum_{i=1}^{n} \mu_{i,j} \Delta N_m z_i + \sigma_{bj} \Delta A_{bj}. \tag{3.6}$$

Combine the summations to yield

$$\Delta G_{S,j} = \Delta N_m \sum_{i=1}^{n} \left(\mu_{i,b} - \mu_{i,j}\right) z_i + \sigma_{bj} \Delta A_{bj}. \tag{3.7}$$

Here, we define the change in chemical potential of the system as,

$$\Delta \mu = \sum_{i=1}^{n} \left(\mu_{i,b} - \mu_{i,j}\right) z_i \tag{3.8}$$

It is also convenient to define the change in chemical potential in terms of activities, α, given by equation

$$\Delta \mu = RT \prod_{i=1}^{n} \ln \left(\frac{\alpha_{i,b}^{z_i}}{\alpha_{i,j}^{z_i}} \right). \tag{3.9}$$

Note that in equation 3.9 the standard states cancel each other assuming that the states used for the solid and liquid phases are consistent. Finally, parameterize both N_m and A_{bj} in terms of radius by assuming the nucleate is a perfect sphere,

$$\Delta G_{S,j} = \pi \frac{4}{3} \frac{r_{bj}^3}{\nu_j} \Delta \mu + \sigma_{bj} 4 \pi r_{bj}^2, \tag{3.10}$$

where ν_j is the molar density of the condensed phase.

Equation 3.10 is often the starting point for CNT. This equation describes the free energy space of the system forming a nucleate of size r of phase j, encased in the bulk phase b. The energy in this space has a maximum value and is an energy barrier that must be overcome for nucleation to occur. This maximum is referred to as the critical Gibbs energy, $\Delta G_{S,j,crit}$ which occurs at the critical radius $r_{bj,crit}$.

To find the critical radius, which corresponds with the maximum $\Delta G_{S,j}$, first take the derivative of equation 3.10 with respect to the nucleates radius. This operation yields

$$\frac{d\Delta G_{S,j}}{dr_{bj}} = 4\pi\frac{r_{bj}^2}{\nu_j}\Delta\mu + \sigma_{bj}8\pi r_{bj}. \tag{3.11}$$

Next, setting the $d\Delta G_{S,j}/dr_{bj} = 0$ and solving for r_{bj} computes the radius that corresponds to the maximum value of $\Delta G_{s,j}$ on the free-energy curve given by equation 3.10. Doing so computes the critical radius given by

$$r_{bj,crit} = \frac{2\sigma_{bj}\nu_j}{\Delta\mu}. \tag{3.12}$$

This equation is then substituted into Equation 3.10, and is used to solve for the maximum $\Delta G_{S,j}$, or the critical change in Gibbs free energy due to nucleation, resulting in

$$\Delta G_{S,j,crit} = \frac{16\pi}{3}\frac{\sigma_{bj}^3\nu_j^2}{\Delta\mu^2}. \tag{3.13}$$

This equation describes the amount of Gibbs free energy that must be overcome to create a stable nucleate.

The next step in the derivation is to describe the pre-nucleation distribution in terms of the free-energy from Equation 3.10. While all of these details are not included a basic framework is presented. First, the series of chemical equations describing the chemical reactions between each pre-nucleation cluster and monomer unit is shown

$$[\omega_{\mathrm{i}}] + [\omega_{1}] \underset{k_{r,i}}{\overset{k_{f,i}}{\rightleftharpoons}} [\omega_{\mathrm{i+1}}]. \tag{3.14}$$

Next, consider a series of equations for each discrete cluster size ranging from 1 to size c. The flux from over this given range can then be described by

$$\begin{aligned} J_1 &= [\omega_1][\omega_1]k_{f,1} - [\omega_2]k_{r,1}, \\ J_2 &= [\omega_2][\omega_1]k_{f,2} - [\omega_3]k_{r,2}, \\ &.... \\ J_c &= [\omega_c][\omega_1]k_{f,c}. \end{aligned} \tag{3.15}$$

The final equation in the series is assumed to be irreversible, and corresponds to Equation 3.2. Note that J_i is a *flux* and not the time rate of change of species ω_{i+1}, but is the reaction rate corresponding to a single chemical reaction. At steady state, the flux J_i is constant and does not change across the pre-nucleation distribution hence it is assumed that

$$J_1 = J_2 = ... = J_c = J_{nuc}. \tag{3.16}$$

Due to the steady-state assumption, J_{nuc} is the nucleation rate of stable particles. J_{nuc} is solved recursively combining the series of equations represented by Equation 3.15: Doing so yields equation

$$J_{nuc} = \frac{[\omega_1]}{\sum_{i=1}^{c} \frac{1}{k_{f,i}[\omega_i]} \frac{k_{r,1}[\omega_2]k_{r,2}[\omega_3]...k_{r,i-1}[\omega_i]}{k_{f,1}[\omega_1]k_{f,2}[\omega_2]...k_{f,i-1}[\omega_{i-1}]} \left(\frac{1}{[\omega_1]}\right)^{i-1}} \tag{3.17}$$

The details of this operation are not included and can be found in Ref. [45]. The same reference uses the assumption of equilibrium to compute the concentration of critical nucleates, $[\omega_{\mathrm{c}}]$, which is equal to

$$[\omega_c] = [\omega_1] \exp\left(\frac{-\Delta G_c}{RT}\right). \tag{3.18}$$

Combining Equations 3.18 and 3.2 yields

$$J_{nuc} = k_{f,c}[\omega_1]^2 \exp\left(\frac{-\Delta G_c}{RT}\right) Z_f. \tag{3.19}$$

Here, the critical Gibbs free energy, ΔG_c, can be computed using Equation 3.13. The Zeldovich factor, Z_f, adjusts for the dynamic behavior of nucleation and is computed as

$$Z_f = \left(\frac{\Delta\mu^2}{12\pi k_b T \Delta G_{crit}}\right)^{1/2}. \tag{3.20}$$

In equation 3.19, the nucleation rate can be solved for in terms of physical constants, the monomer concentration, $[\omega_1]$, and the forward rate constant. The monomer concentration can be obtained from equilibrium chemistry, and the rate constant $k_{f,c}$ can be obtained using analytical expressions given the following assumptions. In the case of diffusion-limited growth of nucleates the following equation equation can be used,

$$k_f = 4\pi r_c D_D, \tag{3.21}$$

where r_c is the critical nucleation radius and D_D is the monomer-binary-diffusion coefficient. For a system where interface-transfer-limited nucleation governs nucleation, Equation 3.22 holds:

$$k_f = 4\pi r_c^2 \frac{D_I}{\lambda}, \tag{3.22}$$

Here, D_I is the interface-diffusion coefficient and is approximated using

$$D_I = \lambda^2 \nu_f \exp\left(\frac{-\Delta U}{k_B T}\right). \tag{3.23}$$

Here, λ is the mean free path of the liquid, assumed to be 2.5 angstroms, v_f is the vibrational frequency, approximated as $k_b T/h_p$, where h_p is Planck's constant, T is the absolute temperature, k_b is the Boltzmann constant and ΔU is the hydration energy [42,45], or energy of activation for interface transfer [46].

In practice, ΔU is difficult to measure and is usually equated to the energy of activation for diffusion [46]. By so doing, one ignores any steric inhibitions at the interface. Heuristics provided by Markov are used to estimate the value of ΔU [45]. ΔU values typically range from 10 to 20 kcal/mol for aqueous salts. This work uses $\Delta U = 10$ kcal/mol.

The computation of the nucleation rate, in Equation 3.19, is contingent upon the following assumptions:

- the system remains at constant temperature and pressure.
- the particles formed are perfect spheres.
- the particles nucleate at rates much slower than diffusive time-scales and faster than other chemical scales, or that the bulk phase chemical potential is constant over the course of the nucleation process.
- the interfacial energy, σ_{bj}, is constant with particle size which, for water droplets it was found to not be [47].
- prenucleation particles increase in size only by single monomer addition.
- only a single phase precipitates.

The above equations are used to compute the steady-state nucleation rate. However, due to the broad range of time-scales found in nucleation, the nucleation rate may not reach the steady state nucleation rate due to a decrease in the driving force of the system. Due to this, it is important to understand the dynamic ramp-up behavior of nucleation. Kashchiev [46] formulated an infinite sum to describe this phenomenon in terms of the steady state nucleation rate, J_{nuc}, given by equation

$$J(t) = J_{nuc}\left(1 + 2\sum_{i=1}^{\infty}(-1)^i \exp\left(-i^2\frac{t}{\tau}\right)\right), \tag{3.24}$$

where t, is time, and τ is defined as the time that it takes to reach approximately 1/3 of the steady state nucleation rate. This sum has poor convergence at short times, or large values of τ and as a consequence, empirical replacements have been suggested [46]. τ can be estimated using

$$\tau = \frac{16}{\pi k_{f,c}[\omega_1]} \left(\frac{\Delta G_{S,j,crit}}{\Delta \mu} \right)^2 \tag{3.25}$$

(See Ref. [45].)

For amorphous calcium carbonate the interfacial energy is not available in the scientific literature. Also there exists a broad range of values for other polymorphs in the calcium carbonate system. Due to this, the surface energy is adjusted to match experimental data.

3.1.2 Classical Heterogeneous Nucleation Theory

Heterogeneous nucleation occurs on the surface of foreign particulates in a given system, and is known to dominate at lower supersaturation ratios. This is somewhat ambiguous as the transition from heterogeneous nucleation to homogeneous nucleation for the barium sulfate system occurs around a supersaturation ratio of 1,000,000 [48].

Heterogeneous nucleation operates on the same assumptions as homogeneous nucleation, however with a smaller value for the critical Gibbs-free energy, ΔG_{crit}, which is achieved by being in proximity to the foreign surface. The decrease in energy due to being adsorbed onto a such a surface is given by,

$$\Delta G_{crit,het} = \Delta G_{crit,hom} \frac{(2 + \cos\theta)(1 - \cos\theta)^2}{4} \tag{3.26}$$

where θ is the wetting angle between the condensed-phase, the bulk-phase, and the foreign particulate. Molecular collisions of monomer units with prenucleation clusters are also modeled differently. Collisions from monomers in the bulk phase as well monomers adsorbed onto the foreign surface are considered. The corresponding reactions are shown in the chemical equations,

$$[\omega_{\mathrm{c,a}}] + [\omega_1] \xrightarrow{k_{f,c}} [\omega_{\mathrm{c+1,a}}], \tag{3.27}$$

$$[\omega_{\mathrm{c,a}}] + [\omega_{\mathrm{1,a}}] \xrightarrow{k_{f,c,a}} [\omega_{\mathrm{c+1,a}}]. \tag{3.28}$$

Here, the subscript, a, denotes that the species is adsorbed onto the surface. The entire presentation of the computation of heterogeneous nucleation rates is omitted. For the purposes of this work it is sufficient to say that the heterogeneous nucleation rate is equal to the sum of the kinetic rates from Equations 3.27 and 3.28, and is discussed in detail by Schubert and Mersmann [48].

3.2 Meso-Crystal Nucleation

There are many precipitation processes that are not described by classical theory [20, 49]. Classical-nucleation theory is sometimes considered inaccurate because it assumes that particles are spherical and that particles grow only by single monomer addition [19, 49, 50]. The nucleation models presented in this section, referred to as meso-crystallization models, do not rely on either assumption.

Calcium carbonate has recently began being classified as a meso-crystal. Meso-crystallization is a multi-step precipitation process that has recently begun development [51]. Meso-crystals are known to undergo nanoparticle nucleation, aggregation, growth, and re-precipitation as more stable solid phases. A detailed theory for meso-crystallization is still in its infancy and currently only a rough understanding of the kinetic pathways has been established [51]. Consequently, meso-crystallization theory currently does not provide a mathematical framework for the prenucleation distribution, nucleation rates, induction times, etc. Currently, the mechanistic pathways of meso-crystals are being highlighted as different from the classical nucleation mechanics [1, 12, 17, 51].

In this work, two preliminary models for nucleation of meso-crystal precursors are developed and applied to the calcium carbonate system to describe ACC nucleation. Both models use collision mechanics of prenucleation clusters to predict the nucleation rates. One model assumes a simple monodispersed distribution of prenucleation clusters. The other model makes two key assumptions. The first of these assumptions is that the particles form molecular chains, which do not collapse to sphere-like structures until the aggregation/nucleation process occurs. The second assumption is that the prenucleation clusters are in equilibrium with each other.

In accordance with molecular simulation and experimental data [1, 26], it is assumed that a steric energy barrier exists which inhibits the growth of prenucleation clusters, but is overcome via aggregation. The steric environment of a nucleate is the local chemical environment and often differs from the bulk solution. Once aggregation moves molecular clusters past the steric energy barrier blocking growth, they are then classified as particles and are free to grow. The newly formed particles are represented by the particle density function which is subject to growth. This treatment of calcium carbonate clusters is the framework used to model meso-crystal nucleation in this work. Note that referring to this framework as a meso-crystallization model is somewhat of a misnomer since ACC is not a meso-crystal, but is a meso-crystal precursor.

The meso-crystallization nucleation model used here takes an approach comparable to classical nucleation. The smallest clusters are assumed to be in equilibrium with each other and the liquid phase. The nucleation rate is determined using the molecular cluster-size distribution. This approach is desirable because it avoids having to kinetically evolve the molecular-cluster distribution since molecular interactions operate on fast time-scales and require small time steps to temporally resolve the distribution. Consequently, an equilibrium assumption is made for the small clusters, which is used to predict the nucleation rate.

For the prenucleation clusters, two different equilibrium distributions are assumed in this work. The first assumption is based on the observation from Gebauer et al. [1] of a stable ACC particle size of 2.0 nm in diameter. Using this observation, it is empirically assumed that all the prenucleation clusters are distributed at this meta-stable size and that particle aggregation creates nucleated particles. The second assumption utilizes a Gibbs energy correlation from Demichelis et al. [19], which is used recursively to predict the equilibrium cluster distribution. The correlation computed the Gibbs energy of formation of ions linking into chains, hence this approach explicitly assumes that prenucleation embryos consist of molecular chains rather than spheres. Both approaches model nucleation without the use of the supersaturation ratio or a reference point for equilibrium. Also, both nucleation models are paired with interface-limited growth mechanisms for post-critical nuclei, where ΔU is equal to 10 kcal.

3.2.1 Monodispersed Distribution

The computation of the monodispersed distribution needed for the meso-crystal nucleation rate is performed using

$$N_s = \frac{3}{4}\frac{[\mathrm{CaCO_3^o}]\nu_o}{\pi r_n^3}, \tag{3.29}$$

where N_s is the prenucleation-cluster density, and r_n is the radius of the nanoparticles, which is assumed to be a constant value of 1 nanometers based on experimental observation [1]. The computation of the nucleation rate, based on aggregation theory, is given by

$$J = N_s^2 \beta \phi. \tag{3.30}$$

Here, ϕ is the probability of a particle interaction resulting in aggregation and β is the collision rate based on Brownian motion (defined later this chapter). The value of ϕ is set to 1 for classical and meso-crystallization cases (Section 3.2.2). For the monodispersed distribution ϕ is evaluated as

$$\phi = \exp\left(\frac{-\xi \sigma_w \pi r_s^2}{k_b T}\right), \tag{3.31}$$

where, σ_w is the surface tension of liquid water, and r_s is the radius of the smaller of the two aggregates. Equation 3.31 is derived using an approximation computing the energy of dehydration of molecule in solution (see Ref. [52]). Since this approach is a rough approximation, the parameter ξ is tuned to $\xi = 0.7$ to adjust for the approximation at a pH of 10.0, when comparing the model to data found in Ref. [1].

3.2.2 Equilibrium Distribution

In order to predict the distribution function for the equilibrium model, it is assumed that the calcium carbonate complex, $\mathrm{CaCO_3^o}$, represents the sum of all molecular clusters (or bound ions) as

$$[\mathrm{CaCO_3^o}] = \sum_{i=1}^{n} i[(\mathrm{CaCO_3})_i]. \tag{3.32}$$

Here, $[(\mathrm{CaCO_3})_i]$ is the concentration of clusters containing i monomer units and n corresponds to the size where the molecular cluster is assumed to collapse to a sphere. The equilibrium distribution is predicted by

$$[(\mathrm{CaCO_3})_\mathrm{i}] = K_{eq}^{i-1}[(\mathrm{CaCO_3})_1]^i, \tag{3.33}$$

which recursively computes the equilibrium concentration of a cluster of size i. K_{eq} is the equilibrium constant for all cluster sizes based on the Gibbs energy value of 21.7 kJ/mol from Ref. [19] corresponding to the reaction

$$[(\mathrm{CaCO_3})_\mathrm{n}] + [(\mathrm{CaCO_3})_1] \rightleftharpoons [(\mathrm{CaCO_3})_\mathrm{n+1}]. \tag{3.34}$$

Since $[(\mathrm{CaCO_3})_1]$ is not known, the use of Equation 3.32 is used to create a polynomial of order n in terms of $[(\mathrm{CaCO_3})_1]$. This n^{th} order polynomial only has a single real and non-negative root, which was computed using Newton's method. This root corresponds to the equilibrium concentration of $[(\mathrm{CaCO_3})_1]$.

The nucleation rate relies directly on the distribution of prenucleation clusters,

$$J_{ij} = N_a^2 \sum_{i=n/2}^{n-1} \sum_{j=i}^{n-1} \beta(r_i, r_j)[(\mathrm{CaCO_3})_i][(\mathrm{CaCO_3})_j]\phi. \tag{3.35}$$

Equation 3.35 represents the aggregation of all prenucleation embryos $n/2$ and larger. Consequently, several different sizes are nucleated into the particle distribution, all of which are larger or equal to size n.

Equation 3.35 is used in this work, however, a simplified equation may be used which introduces a minor error by assuming only size $n/2$ aggregates. The equilibrium distribution decays exponentially and consequently the $n/2$ size is the primary contributor to nucleation. Per these assumptions, Equation 3.35 can be approximated as

$$J = N_a^2 \beta(r_{n/2}, r_{n/2})[(\mathrm{CaCO_3})_{n/2}][(\mathrm{CaCO_3})_{n/2}]\phi. \tag{3.36}$$

Substituting Equation 3.33 into Equation 3.36 yields

$$J = N_a^2 \beta(r_{n/2}, r_{n/2}) K_{eq}^{n-2}[(\mathrm{CaCO_3})_1]^n \phi. \tag{3.37}$$

Due to the lack of theory describing the stable critical size, n, it is adjusted to fit data sets at a pH of 10.0. For calcium carbonate a value of $n = 36$ was found, which corresponds to a spherical radial size of 9.1 nm.

3.3 Growth

A wide variety of studies have been conducted on the growth of calcium carbonate systems, however these papers are often at concentrations much lower than considered here, hence theoretical models are used. Particle growth is assumed to follow two different expressions: diffusion-limited growth [53], and interface-limited growth [46], given, respectively, by

$$G_D(r) = \frac{D_D C_{eq}(S-1)\nu_o}{r}, \tag{3.38}$$

$$G_I = D_I C_{eq}(S-1)\left(\frac{3}{4}\pi^{1/2}\nu_o\right)^{2/3}. \tag{3.39}$$

Here, $D_D = 6.63 \times 10^{-10}$ m^2/s and is the diffusion coefficient of monomer (calcium carbonate ion pair), C_{eq} is the equilibrium concentration of monomer with respect to the solid phase, S is the supersaturation ratio, ν_o is the solid-phase molar volume and D_I is defined above.

The net growth rate is assumed to be limited by the slower of the two growth expressions, as described by

$$\frac{dr}{dt} = \left(G_I(r)^{-1} + G_D(r)^{-1}\right)^{-1}. \tag{3.40}$$

This equation assumes that the processes occur in series.

3.4 Aggregation

Aggregation is the combination of smaller particulates that collide to form a larger particle. Aggregation is conventionally modeled using a collision frequency term, β, and the efficiency factor ϕ. The driving forces for aggregation are often attributed to Brownian motion, differential settling, laminar shear, and turbulence.

Each of the above mechanisms rely on different physical processes to create particle collisions. Brownian motion of particles is due to atomistic collisions between atoms and particles. This results in erratic motion of the small particles. Differential settling is caused by gravitational or centrifugal effects causing large particles to settle faster than small particles, resulting in collisions [33]. Laminar shear causes collisions due to colloidal particles following the velocity profile which is not uniform and hence results in collisions. Collisions due to turbulent flow results from particles being large enough such that they have inertial movement.

The collision rate, β, due to Brownian diffusion can be computed as

$$\beta_B(r, R) = \frac{2k_bT}{3\mu}\frac{(r+R)^2}{rR}, \tag{3.41}$$

where μ is the fluid's dynamic viscosity [33]. Note that this Brownian collision model predicts that two 1-meter sized sized particles are just as likely to collide as two nano-particles. This is because the nano-particles are much smaller, reducing the chance of a collision, although their mean Brownian velocity is much higher. Consequently, particles disparate in size have the highest collision frequency.

The collision rate due to differential settling can be computed using

$$\beta_S(r,R) = \frac{2\pi g}{9\mu}(\rho_s - \rho_f)(r+R)^3\left|r-R\right|. \tag{3.42}$$

Here, g is the acceleration due to gravity, ρ_s is the density of the particle and ρ_f is the density of the fluid. The value of g could be replaced or altered to account for centrifugal effects.

The particle collision rate due to laminar fluid shear is described by

$$\beta(r,R) = \frac{4}{3}(r+R)^3\frac{\partial u_f}{\partial x}, \tag{3.43}$$

where u_f is the fluid velocity [33]. Here, the underlying assumption is that the particles are small or colloidal. The spherical particles therefore follow the flow velocity perfectly and the velocity gradient causes particles to move at different rates, resulting in collisions. The term du_f/dx is approximately equal to 5 s^{-1}, for slow stirring in a beaker [33].

For turbulent systems the kinetic energy can be used to predict particle collisions given by

$$\beta(r,R) = \frac{4}{3}\left(\frac{3\pi}{10}\right)^{1/2}\left(\frac{\epsilon\rho_f}{\mu}\right)^{1/2}(r+R)^3, \tag{3.44}$$

Here, ϵ is the turbulent-kinetic energy dissipation rate [54], and is ideal for $k-\epsilon$ turbulent models where ϵ is transported directly. It is assumed that Equation 3.44 dominates for large particles while Equations 3.41, 3.42, and 3.43 describe colloidal particles.

The collision efficiency parameter, ϕ, has simple heuristics for estimating it. In general, the more stable the colloid the lower the efficiency factor. The efficiency factor is therefore low for stable colloids, such as fresh water colloids, 10^{-3} to 10^{-6} and and high for colloids in sea water, $0.1 - 1.0$. Semi-empirical approaches to computing ϕ have been studied [55].

Once the aggregation efficiency and the collision frequency are computed, the aggregation rate of a radial distribution can then be computed. Equation 3.45 computes the rate of aggregation of particles with a radial particle density function, $\eta(r)$:

$$\frac{\partial \eta(r)}{\partial t} = \frac{r^2}{2} \int_0^r \frac{\beta\left(\left(r^3 - R^3\right)^{1/3}, R\right)\phi}{\left(r^3 - R^3\right)^{2/3}} \eta(R) dR - \eta(r) \int_0^\infty \beta((r, R)\phi\eta(R) dR \tag{3.45}$$

Here, $\beta(r, R)$ is the collision frequency of particles with radius, r with all other particles of size R, and ϕ is the efficiency factor. Note that similar equations can be formulated using mass based or volumetric particle density functions.

3.5 Calcium Carbonate Equilibrium Model

In order to compute the monomer concentration $[\omega_1]$ used in the above nucleation models, calcium carbonate concentrations must be computed. To do this, the aqueous system is assumed to be in equilibrium since aqueous reactions are much faster than mixing and precipitation processes. The equilibrium chemistry of calcium carbonate can be modeled using several experimental equilibrium correlations provided in Refs. [2, 4, 56]. Equilibrium among the following nine species is considered: H^+, OH^-, CO_3^{2-}, HCO_3^-, $\mathrm{H}_2\mathrm{CO}_3^*$, Ca^{2+}, CaHCO_3^+, CaOH^-, and CaCO_3^o.

The Davies activity coefficient formulation is used in this work to maintain consistency with the equilibrium correlations which were developed using the Davies equation [4]. The expression for Davies based activity coefficients is given as

$$\log_{10}(\gamma_i) = -A z_i^2 \left(\frac{\sqrt{I}}{1 + \sqrt{I}} - 0.3I\right), \tag{3.46}$$

where, I is the ionic strength of the solution defined previously, z_i is the charge of a species i, γ_i is the activity coefficient of species i, and A is a constant that depends on the solvent (in this work A is equal to 0.508 at 24 ^{o}C [33]).

This equilibrium model was compared to experimental data [57] of calcite solubility versus sodium chloride concentration at 25 ^{o}C, with good agreement. The model was compared to the Pitzer formulation showing approximately a 1% and 10% difference in the calcium ion concentrations at a pH of 9.0 and 10.0 respectively. Other studies have shown that for a solution with an ionic strength less than $I = 0.1$, less than 10% difference is reported in the supersaturation ratio for calcium carbonate [58]. Additionally, the ionic strength considered here remained less than $I = 0.1$, for which case the Davies thermodynamic model is sufficient.

Chapter 4. Results

This chapter presents simulation results using the physical models described in previous chapters. Four different nucleation models are investigated. This is done to show, that classical nucleation manages to describe the nucleation behavior of this system, despite claims otherwise [1]. The simulation results are discussed and compared to data measured by Gebauer et al. [1].

4.1 Chemical Analysis

The equilibrium model described in by Plummer and Busenberg [4] was applied to the experiment conducted by Gebauer et al. [1] by temporally evolving elemental concentrations. Simulations using exclusively the equilibrium model, without a solid kinetic model showed good agreement with the data in the pre-nucleation Stage I.

It is expected that the stand-alone equilibrium chemistry model simulating the chemistry of the batch reactor should have good agreement with experimental data prior to nucleation. Figure 4.1 shows temporal profiles of calcium ions present in solution generated by the equilibrium model alone, without a solid chemistry model included. The initial rise in calcium concentration corresponds to the slow addition of calcium solution, shown by both the model and experiment. There is a slight difference between the total calcium dosed and the amount measured by the calcium-selective probe due to chemically-bound calcium ions. The drop of the solid lines is due to the precipitation process and the corresponding mass of calcium ions in solution are at nearly equilibrium values due to pseudo-steady-state growth.

The slopes of the model (dashed lines) and the slopes in Stage I of the experiment, shown in Figure 4.1, show good consistency at low pH values. However, the model overesti-

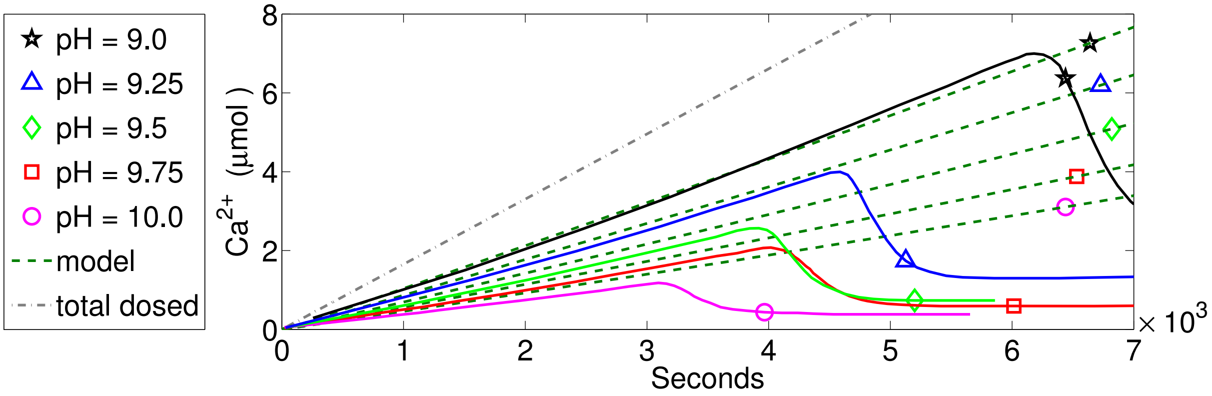

Figure 4.1: A parametric study in pH of calcium ion concentration as a function of time comparing simulation (dashed lines), ignoring solid-phase chemistry, with experimental results [1] (solid lines). Only 5 of 15 experiments are included for visual clarity. The upper dashed-and-dotted line is the total moles of calcium ions added to the system. These simulation results without the solid chemistry model are expected to only capture the rise of calcium ions.

mates the free ion concentration by up to 20% at high pH. The overestimation of free-calcium ions in solution may be due to:

- Carbon dioxide absorption is more prominent at high pH values, an effect that would increase the fraction of bound-calcium ions.
- Gebauer et al. [1] did not use an activity model, hence differences in the activities due to the change in ionic strength between the calibrated solution and the system of interest would result in a decrease in measured free-calcium-ion activity.

The equilibrium model presented is shown to have good agreement despite the discrepancy at high pH values.

The solid phase kinetics for ACC precipitation are not well established. Due to this, an empirical solid phase model termed a nucleation pulse, was also considered for the precipitation of ACC particles. The nucleation pulse allows that chemical state and equilibria could be traced throughout the experiment. This is advantageous for comparing various solid-phase kinetic models without the added complexity of the equilibrium chemistry. The

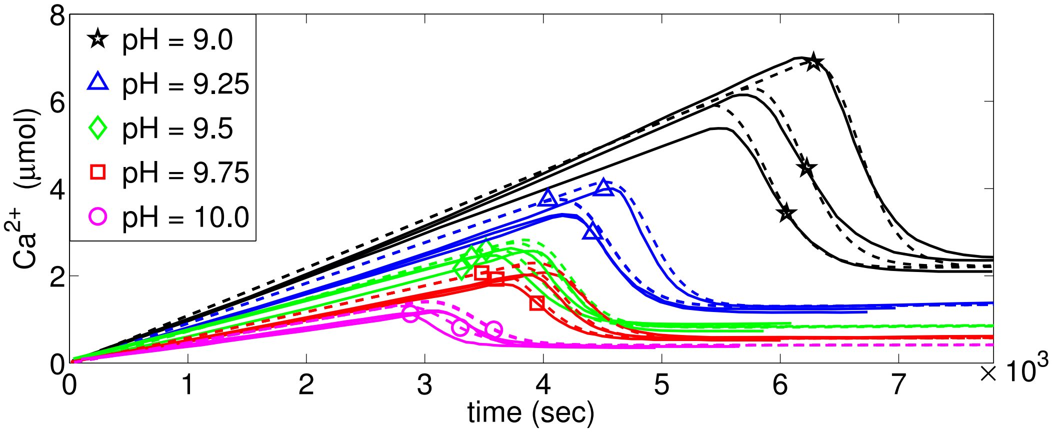

Figure 4.2: Comparison of the equilibrium model using the artificial pulse (dashed lines) with experiment [1] (solid lines), used as a baseline for chemical analysis.

empirical solid phase model consists of an empirical nucleation rate (assuming 10 nm diameter particles) coupled with diffusion-limited growth. The amount of particles dosed was contingent upon the correct rate at which the curve decreases. Using this approach, the lower limit of experimental deviation from ACC equilibrium due to kinetic effects (referred to as the equilibrium offset) is quantified and is described in more detail below.

The solid lines in Figure 4.2 show the total calcium ions in solution for 15 of the Gebauer experiments, which consisted of three replicate experiments at five different pH values. The dashed lines show the calcium trace generated by the nucleation pulse, which is intended to trace the experimental data. The nucleation empiricism shows sufficient agreement to capture temporal traces of chemical species. The use of a nucleation pulse was preferred to forcing the calcium ions in the model to equal the reading from the calcium probe to allow for better comparison between models.

The use of a nucleation pulse in combination with a finite diffusion-limited growth rate quantify the minimum offset of the equilibrium value in Stage III of the experiment. This offset is the deviation of the equilibrium IAP above the actual equilibrium point. The offset is due to the continual dosing of calcium ions in the experiment creating a higher apparent equilibrium ion activity product due to the finite growth of ACC particles. Using diffusion-limited growth allows the computation of the minimum offset, because diffusion-limited growth limits other growth mechanisms due to steady-state radial concentration profiles.

Applying the equilibrium model directly to the calcium concentrations presented in Ref. [1] at 24 ^{o}C operates on the assumption of infinitely fast growth kinetics. Hence, Figure 4.3 shows two equilibrium values for ACC solubility, one assumes infinitely fast growth, the other assumes finite growth kinetics, $\log_{10}(K_{eq}) = -7.67$ and $\log_{10}(K_{eq}) = -7.74$, respectively. ACC and vaterite solubility values are also included in Figure 4.3 to show how this variant of ACC differs from conventional ACC. Additionally, the two values reported in Ref. [1] are included in the figure.

It is worth noting that the disparity between the above equilibrium constants, shown in Figure 4.3, differ by factor of 2.1 to 1.45. In general the values here are lower by taking into account non-idealities in the chemistry as well as accounting for steady state growth. The former of these two phenomenon accounts for 85% of the discrepancy. This means that the disparity between the equilibrium values reported here and in Ref. [1] is primarily due to the inclusion of an activity coefficient model, and to a lesser extent accounting for finite growth kinetics. This results in an equilibrium constant for ACC that is 45% higher than the equilibrium concentration of vaterite and an order of magnitude lower than conventional ACC.

It is unclear as to how Gebauer et al. [1] concluded that two discrete equilibria existed based on the data published. There are a few possible explanations for the discrepancy. The ionic strength increased with increasing pH. This may have led to the appearance of different equilibrium values when assuming an ideal system. Also, calibration of the calcium probe was done for each pH independently. While this type of calibration is necessary for accurate measurement of calcium ions, it statistically reduces the number of data points from 15 to 5. This creates the possibility that the differences in the equilibrium values reported in [1] are a possible artifact of calibration.

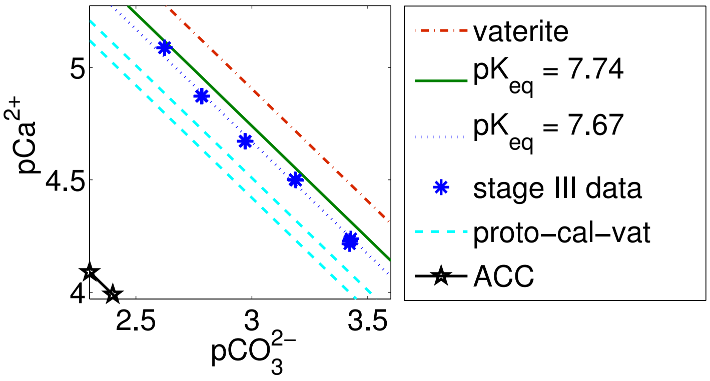

Figure 4.3: Comparison of the several reported equilibrium values for proto-vaterite and proto-calcite ACC at 24 ^{o}C, including vaterite for reference. Here only one value is reported due to little spread in the data. In order of increasing solubility (top right to bottom left), the equilibrium values are: vaterite in Ref. [4], ACC assuming finite growth kinetics, ACC assuming infinite growth kinetics, experimental data [1], two equilibrium values reported in Ref. [1], and a traditional ACC equilibrium value [8].

The chemical composition was also inspected at the time of nucleation. At critical saturation the traditional IAP of calcium and carbonate ions showed the strongest correlation with the data. One set of ions that showed a strong correlation up to a pH of 9.75 was the ion product of $CaHCO_3^+$ and CO_3^{2-}. Figure 4.4 shows that to within the variation of an experiment, once an IAP of 6.5E-9 is reached, precipitation occurs, indicating that this IAP may be used to predict precipitation at low pH. For the highest pH of 10, either the model itself may lack chemical species, or an alternative mechanism may dominate.

4.2 Solid-Phase Kinetics

The experiment conducted by Gebauer et al. [1] was simulated using the equilibrium model combined with the solid-phase kinetic models described in the previous chapters. This was done to investigate four different mechanisms for precipitation: meso-monodispersed, meso-equilibrium, classical-diffusion, and classical-interface nucleation models. These models were coded into Matlab R2009a and compared to the results performed by Ref. [1] at Stages II and III.

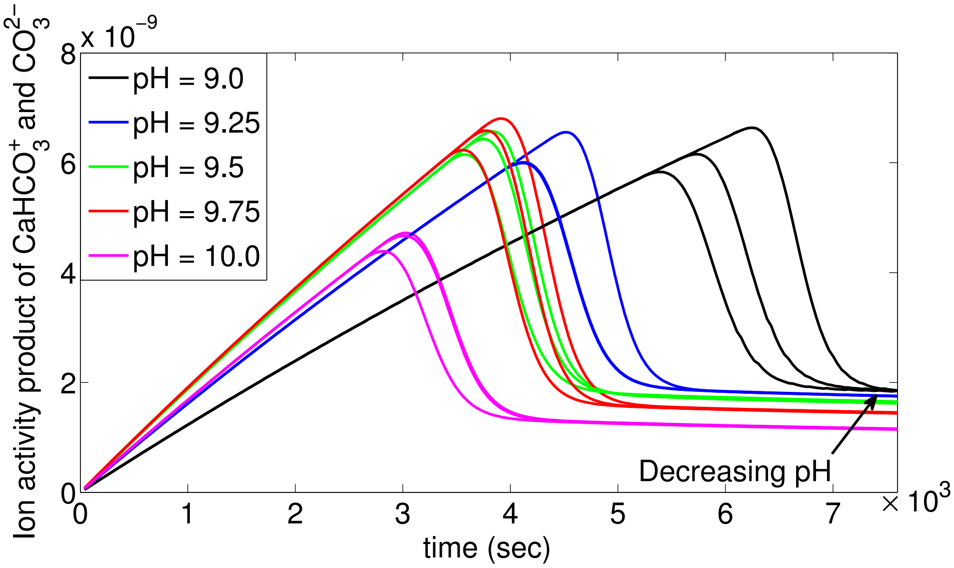

Figure 4.4: The ion-activity products of $CaHCO_3^+$ and CO_3^{2-} as a function of time at a pH of 9.0, 9.25, 9.5, 9.75, and 10.0. The nucleation mechanism used to predict the dynamic IAP of these ions was achieved using the artificial pulse.

Figure 4.5 shows IAP traces for the 15 pH experiments generated by four solid-phase kinetic models. The three distinct stages are present in all the models, exhibiting the initial rise in the IAP due to calcium dosage, the nucleation event, and the steady state growth stage. Note that in Stage III, the IAP is not in perfect equilibrium with the solid phase, but is an over estimate of the solubility due to the constant addition of calcium ions (see Figure 4.3). This effect is amplified by low particle densities and slow growth rates as is illustrated by the disparity between the meso-monodispersed the classical-interface precipitation models.

Key features in Figure 4.5 are plotted in Figure 4.6 to more accurately show key dynamics and features of the models. The upper plot in Figure 4.6 shows the times corresponding to the maximum observed IAP over the course of the simulations. These times are referred to as the time to max IAP and are compared to the corresponding values observed in the experiment [1]. In general, a decreasing trend is observed, which is primarily due to a smaller fraction of calcium being bound at higher pH, hence increasing the time required to reach the the critical IAP. An exception to this occurs at a pH of 9.75 and may be due to the

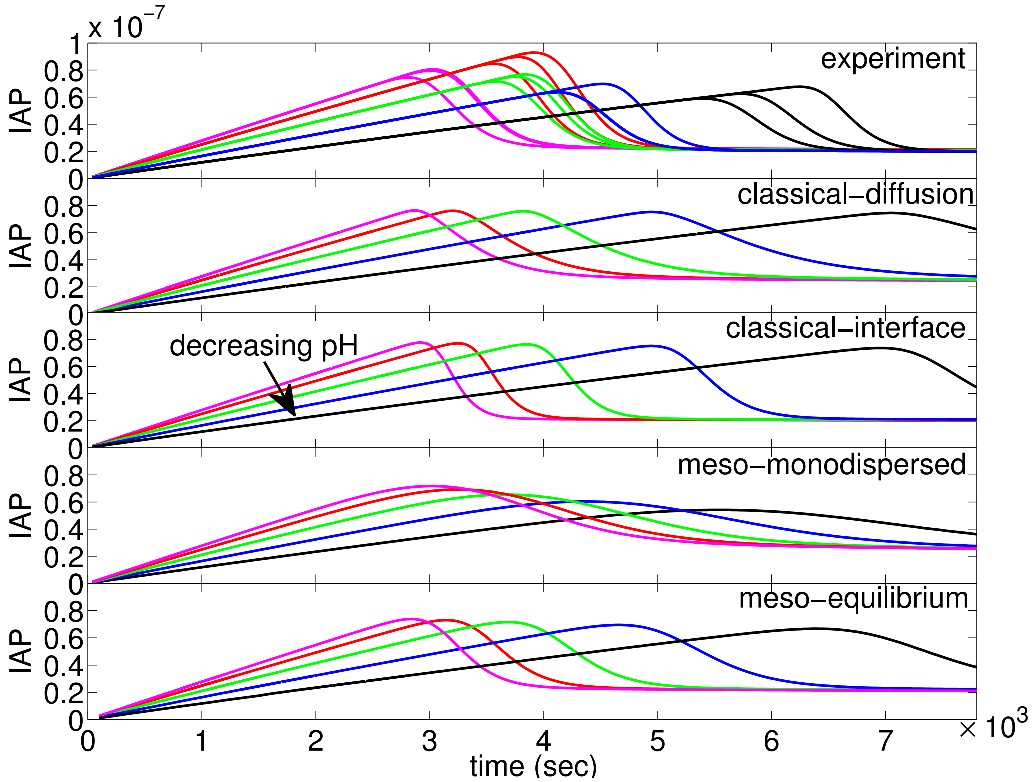

Figure 4.5: The solid lines represent the calcium ions extracted from results by Gebauer et al. [1] at a pH of 9.0, 9.25, 9.5, 9.75, and 10.0. From top first: artificial pulse based on experimental data, using diffusion growth. Second: diffusion-limited precipitation. Third: interface-limited precipitation. Fourth: meso-model with interface-limited growth assuming a monodispersed distribution of prenucleation embryos. Fifth: meso-model with interface-limited growth assuming an equilibrium distribution of prenucleation embryos.

changes in the steric effects not accounted for by the models, i.e. pH dependence of stable size, interfacial energy, or energy of interface transfer. Consequently, none of the models are able capture the time to reach the critical point at this pH. However, under the assumption that pH affects steric conditions, pH sensitive parameters could be introduced to capture the the IAP profiles more accurately. Regardless of pH effects on the steric environment, the models as presented match the data with good agreement without implementing such functionality.

The lower plot of Figure 4.6 shows the maximum IAP reached vs. pH, and in general they are positively correlated. The four solid-phase kinetic models also predict a positive

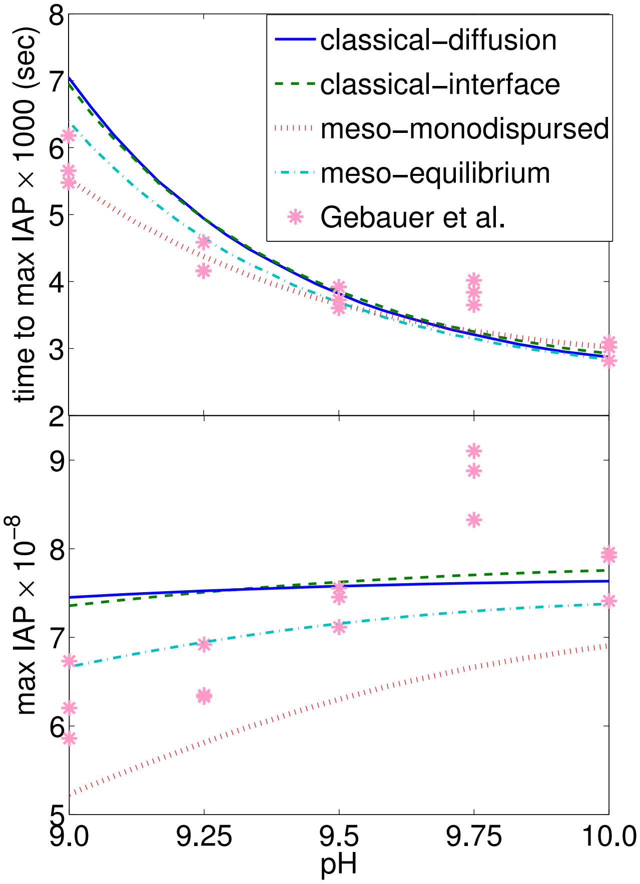

Figure 4.6: Top: time before the maximum IAP is reached for the four solid kinetic models and experimental data as a function of pH. Bottom: the maximum IAP for the four kinetic models and experimental data as a function of pH.

relationship between the maximum IAP and pH. The models have no physics accounting for steric variations due to pH, hence, this positive correlation occurs due to the rate at which the supersaturation ratio increases. Hence, the increasing trend indicates that the rate of calcium addition affects the critical saturation point. However, due to scarcity of data, it is still feasible that the steric effects are responsible for the increase in critical IAP vs. pH. The experimental IAP values reported in Figure 4.6 (represented by asterisks) used the artificial pulse profiles. By doing this, the spread in the three data points was narrowed due to the removal of experimental variation.

Figure 4.7 shows the nucleation-rate dependency on supersaturation for the four solid-phase kinetic models. When plotted against $(\ln S)^{-2}$, the log of classical-nucleation rates are

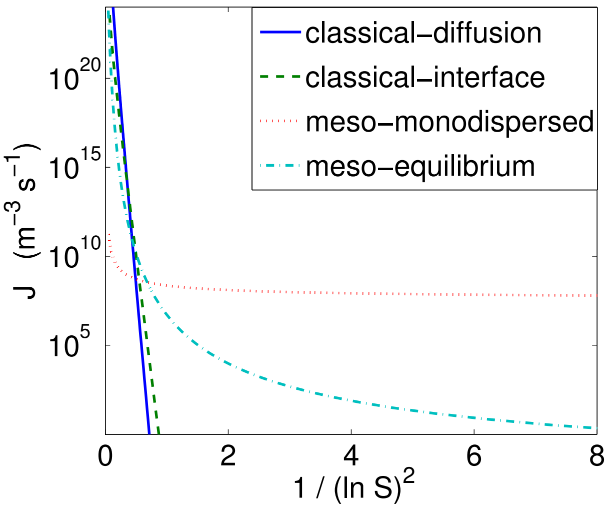

Figure 4.7: Nucleation rate, J, as a function of $(\ln S)^{-2}$ where S is the supersaturation ratio used for the classical models defined in terms of activities using $K_{sp} = 1.80E\text{-}8$ at 24 ^{o}C.

linear. Although the meso-models are not linear, they may be viewed as having two linear regimes. This is a very interesting result, as the meso-models exhibit S dependence similar to what has been observed by experimentalists studying the $BaSO_4$ system [27,48,59,60]. A common approach to modeling the $BaSO_4$ system is to define a homogeneous regime as well as a heterogeneous regime. In distilled water, heterogeneous nucleation is argued to occur due to the presence of trace impurities, and not necessarily at the surfaces of the mixing apparatus [27, 48, 59, 60]. However, this does not explain why heterogeneous nucleation occurs at the same rate in ultra-pure systems as it does in standard distilled water [48]. Hence, nucleation models based on aggregation/collision frequency offer insight concerning this paradox by exhibiting two separate regimes using a single model.

The temporal traces of solid-phase properties for the various particle-phase models at a pH of 10.0 are shown in Figure 4.8. The upper plot shows the particle number density, the middle plot shows the effective nucleation rate, and the lower plot shows the mean particle radius, all as functions of time. In the upper plot, the slight decline after the sharp rise, is due to aggregation. The middle plot shows the nucleation rate coupled with the aggregation term for each of the models. The lower plot shows that the four models predict similar

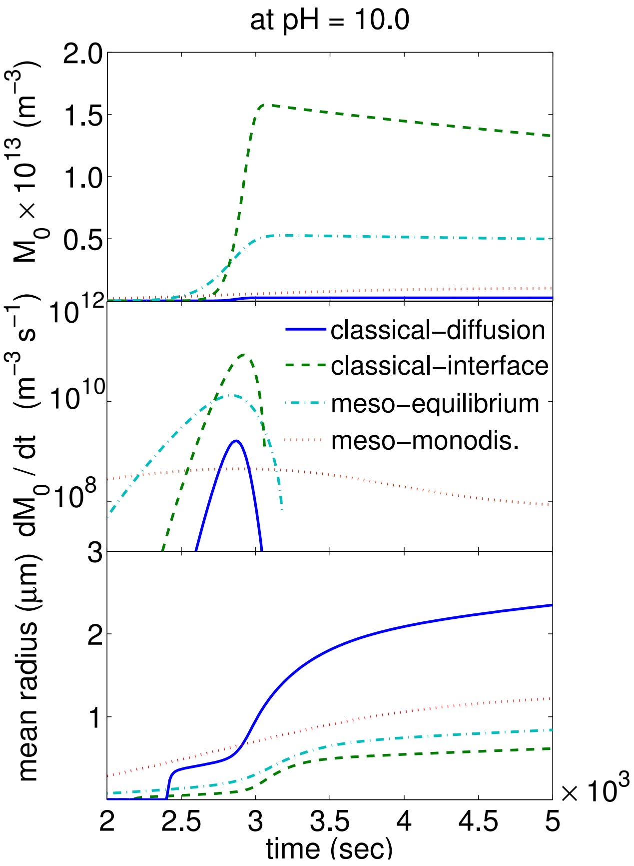

Figure 4.8: Top: particle number density (moment zero). Middle: rate of change of particles on a log scale. Bottom: mean radial particle-size.

values of the mean radial size. This is expected due to mass-balance constraints and the weak geometric relationship of particle volume on particle radius. The particle properties showed little variation over varying pH values, but generally, the simulations predicted larger and fewer particles at lower pH values.

4.2.1 Diffusion-Limited Model

Diffusion-limited growth and precipitation is often expected in an amorphous material due to the high supersaturation ratios and lack of lattice structure, however it was observed that this model poorly reproduced the data in key aspects. As seen in Figures 4.6 and 4.8, this model exhibited essentially a constant critical IAP, and showed very little aggregation. It did however exhibit nucleation-burst behavior (strong supersaturation dependence) expected in a LaMer precipitation experiment and gave reasonable IAP traces.

4.2.2 Interface-Transfer-Limited Model

Interface-limited nucleation had the highest nucleate density and hence exhibited the most aggregation of the four models, which was suggested to occur by Gebauer et al. [1]. Of the two classical nucleation models, interface-limited best describes the system of interest. This is because it matched the data better in the time to max IAP, max IAP, and supersaturation dependence, as well as having a better qualitative fit to the IAP traces (Figures 4.5, 4.6, and 4.7). Both of the classical nucleation models showed similar simulation results, and the differences between them is primarily due to the addition of the parameter ΔU. Because of this, it is possible that increasing the ΔU parameter may result in better agreement with data. However, when increasing ΔU (and after re-tuning the interfacial energy), the particle number density becomes much larger such that aggregation is strongly exhibited. Based off this observation, the performance of this model could be improved by increasing ΔU in combination with a lower collision efficiency for aggregation.

Note that the sensitivity of the equilibrium offset to ΔU is not taken into account in determining the equilibrium value of ACC. The inclusion of ΔU can greatly increase the concentration of calcium ions at which steady-state growth occurs. This would thereby increase the perceived equilibrium concentration of the system, which would lower the actual equilibrium concentration of ACC particles. Hence, as ΔU increases, growth kinetics decrease, resulting in a larger equilibrium offset.

4.2.3 Meso-Monodispersed-Distribution Model

The meso-monodispersed model was designed around the experimental observations found in Ref. [1], that bound calcium exists as particles 2 nm in diameter. A comparison between meso-monodispersed and meso-equilibrium models shows that assuming that the entire distribution is concentrated at a single critical value does not result in the burst nucleation behavior exhibited by the data. Additionally, the particle number density remained too low for aggregation to occur, as was suggested to occur by Gebauer et al. [1]. However, a large number of particles form before the nucleation event, which was observed experimentally, yet the mean size of these particles is much larger than 2 nm as seen in Figure 4.8. While the meso-monodispersed model fails in the above ways, it manages to capture the time to reach the max IAP fairly well (Figure 4.6).

The meso-monodispersed model shows the correct increasing trend in the critical IAP vs. pH (Figure 4.6). Since the kinetic model captures this trend with good agreement, it suggests that the changes in the critical IAP due to pH are caused by kinetic effects rather than steric or thermodynamic effects.

4.2.4 Meso-Equilibrium-Distribution Model

The meso-equilibrium model showed the best overall agreement between the experiment and the models considered here. Good agreement was seen in predicting the peak of the IAP traces, as well as strong dependence on the IAP of calcium and carbonate. Consequently, this model exhibits a nucleation burst, typically observed in a LaMer experiment. Additionally, this model's IAP trace has a similar qualitative shape to that of the IAP generated by the nucleation pulse as, seen in Figure 4.5.

4.2.5 Additional Results

When the presented models are applied to systems where vaterite forms, as in Ref. [2], at lower supersaturations, the models predict the formation of ACC after the experimental observation of precipitated vaterite. This indicates that the precipitation mechanism may produce multiple polymorphs in parallel. However, due to the large induction time of vaterite, the prenucleation embryos are likely undergoing a structural transformation with a time-scale as large as an hour.

Table 4.1: Kinetic constants for classical precipitation models at a supersaturation of $S = 4$.

Solid-Phase Variable	Classical-Diffusion	Classical-Interface
k_f [volume/time]	$4\pi r_c D_D$	$4\pi r_c^2 D_I/\lambda$
ΔU [kcal/mol]	0	10.0
σ [J/m^2]	0.0360	0.0320
k_f at $S = 4.0$ [m^3/s]	9.22×10^{-19}	9.15×10^{-22}
r_c at $S = 4.0$ [m]	1.11×10^{-9}	0.98×10^{-9}
τ at $S = 4.0$ [s]	2.2×10^{-3}	21.5
J at $S = 4.0$ [1/(m^{3}s)]	4.4×10^{7}	3.5×10^{9}
dr/dt at $S = 4.0$ for $r = 10^{-9}$ [m/s]	3.1×10^{-6}	1.3×10^{-8}

Table 4.1 shows some of the key parameters of the classical models. The parameter τ is a time-scale describing the build-up of prenucleation embryos and is calculated using classical nucleation methods [45, 46]. The small value of τ shows that under the assumptions of classical nucleation the dynamic effects of the prenucleation distributions are not important. Note also that taking into account for ΔU has a large influence on τ. The parameter r_c is the nucleation radius predicted by homogeneous classical-nucleation theory [45, 46]. Note that two orders of magnitude exist between the nucleation rate, J, for the two models, which accounts for the large difference in particle number density between the classical models.

The classical models poorly capture the the critical IAP values (Figure 4.6) and also show little aggregation. In defense of the classical theory, the theory is able to fit a single pH with good results, and can be applied to different pH experiments with some predictive ability. Additionally, Table 4.1 shows that the critical radius predicted by classical theory is similar to that observed by Refs. [1, 61], 0.55 to 1 nm. This means that the stable prenucleation embryos observed in experiment are in fact stable according to classical theory as well. Improvement in the classical theory may also be achieved by finding means to measure ΔU, as this parameter plays an important role in the prenucleation kinetics for the models investigated in this thesis.

Parameterizing this system with a larger ΔU is in accordance with Gebauer et al. [1], who states that the surface-energy barrier to nucleation is small and is dictated by some other inhibiting effect. Additionally, other studies [26, 62, 63] have found that the inhibiting steric effects are expected to be larger for crystalline calcium carbonate (calcite, aragonite, and vaterite). Since ΔU can be viewed as a parameter describing inhibiting steric effects, it may be useful for calcium carbonate polymorphs in describing their kinetic polymorphic preference [42]. The results here suggest that a larger ΔU in combination with a lower collision efficiency Φ than that used in this study is more physical.

Solid-phase models other than those discussed in detail were also investigated. Of special interest was a case utilizing the Kelvin equation for growth in combination with interface-limited nucleation [45]. This case showed two orders of magnitude more particles than any model presented here, which quickly aggregated, lowering the particle densities to similar levels as those shown in Figure 4.8. This behavior is due to the zero growth definition at the critical point for classical models in accordance with the Kelvin equation. This approach may also offer valid avenues in describing this complex system.

Chapter 5. Time-Scale Analysis

This chapter discusses approaches to approximate the time-scales of the precipitating system in Ref. [2]. The time-scales of a system are important, because they allow the an analyst to make approximations which simplify the system. In the case of turbulent reactive flows, fast reactions can be approximated as being instantaneous by using an equilibrium model. In the case of slow chemical reactions turbulence scales can be ignored and a batch or plug flow reactor can be used to model the system without introducing much error. Hence, it is important to identify what timescales overlap, because neglecting to do so may result in superfluous and overly extravagant modeling.

5.1 Time-Scale Definitions

Time-scales have several definitions. For the purposes of this work it is defined as an order of magnitude approximation of the time required for a scalar to undergo a change of interest. A simple definition of a time-scale, τ, of a given scalar, x, can be computed using

$$\tau = \left| \Delta x_{max} \left(\frac{dx}{dt} \right)_{max}^{-1} \right| . \tag{5.1}$$

Here, Δx_{max} denotes the change of interest, usually the difference in the scalar before and after a dynamic event and dx/dt_{max} is the maximum time derivative of the scalar throughout the span of the the dynamic event. Despite the simplicity of this approach, it often is the best for approximating time-scales.

Often a system is complex, and a more elegant approach is desired. If a system can be described in terms of a set of ODEs, time scales can be derived from this system. This is done by taking the Jacobian of this system and then solving for the eigenvalues of the Jacobian matrix. The computed eigenvalues represent the relative rates of change of a system, hence their inverses are the time-scales of the system.

For example, take a system of n ordinary equations,

$$\begin{aligned} \partial x_1/\partial t &= S_1(x_1, x_2, ..., x_n) \\ \partial x_2/\partial t &= S_2(x_1, x_2, ..., x_n) \\ &... \\ \partial x_n/\partial t &= S_n(x_1, x_2, ..., x_n), \end{aligned} \tag{5.2}$$

where x_i is a transient scalar and S_i is an arbitrary source term for the scalar. This system can be compiled into a matrix shown by,

$$\mathbf{J}(t) = \begin{bmatrix} \partial S_1(x_1, x_2, ..., x_n)/dx_1 & \partial S_1(x_1, x_2, ..., xn)/\partial x_2 & ... & \partial S_1(x_1, x_2, ..., xn)/\partial x_n \\ \partial S_2(x_1, x_2, ..., x_n)/dx_1 & \partial S_2(x_1, x_2, ..., xn)/\partial x_2 & ... & \partial S_2(x_1, x_2, ..., xn)/\partial x_n \\ ... & ... & ... & ... \\ \partial S_n(x_1, x_2, ..., x_n)/\partial x_1 & dS_n(x_1, x_2, ..., x_n)/\partial x_2 & ... & \partial S_n(x_1, x_2, ..., xn)/\partial x_n \end{bmatrix}. \tag{5.3}$$

Here, $\mathbf{J}(t)$ is the Jacobian of the system. The eigenvalues of this Jacobian are also the inverse of the time-scales of this complex system and correspond to the original system of ODEs.

This approach allows the computation of time-scales of a system, however the computed eigenvalues do not have particular identity, and can be difficult to analyze them beyond their face value. An approach to remedy this is to transport the eigenvalue values directly [64]. Transporting the eigenvalues directly allows the user to avoid sorting an arbitrary list of eigenvalues. The derivative of the eigenvalue $\dot{\lambda}_i$ is computed as,

$$\begin{bmatrix} \dot{\mathbf{\Lambda}} \\ \dot{\lambda}_i \end{bmatrix} = \begin{bmatrix} \lambda_i \mathbf{I} - \mathbf{J} & \mathbf{\Lambda} \\ \mathbf{\Lambda}^T & 0 \end{bmatrix} \begin{bmatrix} \dot{\mathbf{J}}\mathbf{\Lambda} \\ 0 \end{bmatrix}, \tag{5.4}$$

where Λ is the corresponding eigenvector, I is the identity matrix, and T denotes the transpose. The dot denotes derivative with respect to a time (or any desired dimension). Hence, the time derivative of the Jacobian is required. Note that the inversion of the matrix in Equation 5.4 can be ill conditioned if units are not carefully chosen.

5.1.1 Solid-phase Time-Scale Analysis

The experimental work conducted by Ogino et al. [2] was modeled using diffusion limited growth and nucleation, within the framework of DQMOM. As noted in Chapter 1, Ogino et al. monitored the kinetics and polymorphic preference of a quickly mixed system consisting of two ionic solutions. The dynamics of this system were assumed to be very slow and not mixing sensitive because many of the scalars of interest changed over several thousand seconds. The interfacial-surface energies of four polymorphs, ACC, vaterite, aragonite, and calcite were tuned such that the data was accurately reproduced. This process assumed instantaneous mixing.

The eigenvalues and vectors of this system where also transported for analysis. Figure 5.1 shows the eigenvalues as a function of time over the duration of the experiment on a semi-log and log-log scale. The noisy data shown in the second plot of Figure 5.1 is due to use of a numerical Jacobian. Note that the time-scales for the various scalars range from milliseconds to microseconds. This is a wide range for the scalars and, as will be shown hereafter, overlaps with mixing scales.

As mentioned earlier eigenvalues have no specific identity, hence a sensitivity analysis was conducted to determine which mechanisms were causing the fast scales. The sensitivity analysis showed that the growth mechanism were responsible for fastest of these time-scales. This was because nucleation, by definition of the Jacobian, did not directly effect the time-scales of the moments. This was primarily because nucleation was not a function of the particle size distribution.

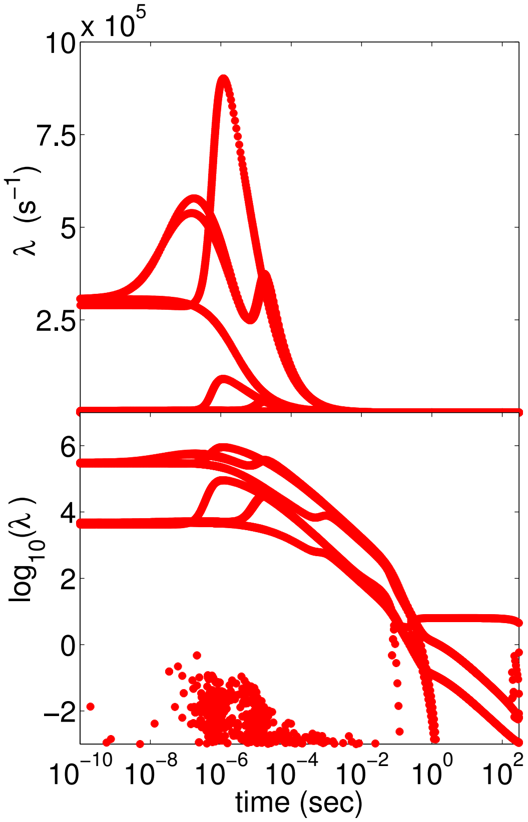

Figure 5.1: Eigenvalues of the Jacobian of a system of ODEs describing the dynamics of an experiment conducted by Ogino et al. [2]

Table 5.1: Time-scales of the particle density, mean particle size, and chemical scalars. These time-scales were defined by Equation 5.1, and are based on theoretical models tuned to fit data from Ref. [2].

Nucleation	Growth	chemical-speciation
35 ms	100ms - 2,500 ms	480,000 ms

A time-scale analysis using Equation 5.1 was also applied the same system. This analysis predicted slower time-scales, which are shown in the Table 5.1.

5.1.2 Turbulence Time-Scale Analysis

Turbulence scales are categorized into three scales which, in order from largest to smallest, are integral, Taylor, and Kolmogorov scales. These scales are used to describe the range of velocity fluctuations within a turbulent system. The Batchelor scale describes the fluctuations of non-velocity quantities, such as temperature, mixture fraction, or species.

The overlap of Batchelor time-scales and reactive time-scales creates the potential for inaccuracies when under-resolving the grid. The ODT model, however, resolves both the velocity scales as well as the Batchelor scales. This means that no mixing model is needed, a key advantage of ODT.

Here, ODT is simply used to compute mixing scales of turbulence for a channel flow with a Reynolds number of 40,000. The initial chemical composition of the ODT-line is set to equal concentrations found in Ref. [2] where the mixing layer lies along the centerline of the channel. A channel flow is an inhomogeneous flow, which results in spatially dependent turbulent mixing time-scales. Despite the presence of a broad range of energy spectra within the flow, only the time-scales at the centerline are considered. This is presumed to be sufficient since the center-line also corresponds to the mixing layer, between the two streams in this particular case.

In order to compute the Batchelor scale along the centerline, several expressions can be used. The smallest Batchelor scale can be defined in terms of the Kolmogorov scale, related by

$$\lambda_B = \frac{\eta}{Sc^{1/2}}. \tag{5.5}$$

Here, λ_B is the Batchelor scale, η is the Kolmogorov scale, and Sc is the scalar Schmidt number. Note that while the length scales of scalars are smaller than velocity fields for high Schmidt numbers, the time-scales are larger, shown by the relation

$$\tau_B = \frac{1}{2}\ln(Sc)\tau_\eta, \tag{5.6}$$

(from Ref. [65].) The definitions of the integral time-scale as well as the Kolmogorov scales are given by,

$$\tau_\eta = \left(\frac{\nu}{\epsilon}\right)^{1/2}, \tag{5.7}$$

Table 5.2: The broad range of mixing time-scales for both velocity and speciation scalars due to turbulence is shown. The values shown are based on a Schmidt number of 850 for a planar channel with a Reynolds number of 40,000. These results were obtained using ODT. All the scales reported here have units of seconds.

Time	τ_ϕ, Batchelor	τ_η, τ_I, Velocity
0	0.001-0.4	0.0005-0.05
.05	0.0035-0.4	0.0012-.075
.4	0.008-0.7	0.002-.07
1.0	0.1-0.6	0.0035-0.1

$$\tau_\phi = \frac{2\left\langle \phi'^2 \right\rangle}{\epsilon_\phi}. \tag{5.8}$$

Here, $\phi^{'}$ is the deviation from the mean mixture fraction, ϵ_ϕ is the scalar dissipation rate and τ_ϕ is the upper limit of the Batchelor time-scale. In Equation 5.7, ν is the kinematic viscosity and ϵ is the the turbulent kinetic energy dissipation rate. These equations used with ODT are used to estimate the mixing scales of the Ogino et al. [2] system operating in a channel flow, with a Reynold number of 40,000. Note that Schmidt numbers vary for the various species included in the chemistry model, ranging from 120 to 1300. The equation used to compute the dissipative term, ϵ_ϕ, is

$$\epsilon_\phi \equiv 2D_\phi \left\langle \left(\frac{\partial \phi}{\partial x} \right)^2 \right\rangle . \tag{5.9}$$

Here, x is the spatial coordinate, D_ϕ is the diffusion coefficient of a given scalar ϕ. Several of the needed values can be obtained from ODT simulations code and are presented in Table 5.2.

5.1.3 Time-scale Overlap

In Sections 5.1.1 and 5.1.2 a broad range of time-scales were shown. When comparing Tables 5.1 and 5.2, significant overlap exists between the Batchelor, nucleation and growth time-scales. This overlap is shown in Figure 5.2. The top half of this figure shows the mixing scales, and the bottom half of this figure shows the reactive scales. V.A.C denotes the structured polymorphs, vaterite, aragonite, and calcite. ACC is kinetically dominant over these polymorphs, which form over a much greater time-span. Due to the time-scale overlap these systems are expected to be influenced by mixing.

Note that the eigenvalue analysis predicts much faster scales than the computing the scales using Equation 5.1. This may be because the eigenvalue analysis captures numeric stiffness in the Jacobian due to transporting moments. This is likely, because the difference in time scales was prominent when switching between QMOM and DQMOM, which were verified to be the same in terms of the moments. Hence, this analysis could be done more accurately, if the moments were deconvolve into mean particle size, variance, particle density, and polymorphic preference.

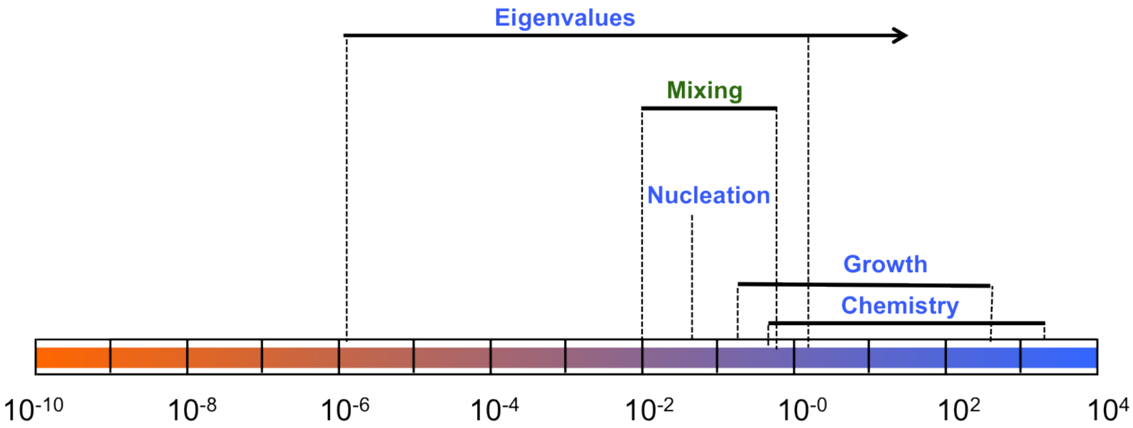

Figure 5.2: Diagram showing the overlapping of time-scales of chemical kinetics and mixing due to turbulence. The mixing scales are denoted in green, ranging from 10 ms to 400 ms. The reactive scales, noted in blue,show a broad range of time-scales, based on different methods. Time-scales for reactive scalars range from one microsecond to several hundred seconds. ACC nominally has faster time-scales. V.A.C. denotes vaterite aragonite and calcite time-scales. The reactive scales are applicable to the experiment conducted by Ogino et al. [2]. The mixing scales are for a planar jet with a Reynolds number of 40,000.

Chapter 6. Conclusions and Future work

At the beginning of this thesis the great extent of uncertainty in understanding aqueous calcium carbonate was presented. This work has aimed to improve fundamental understanding of the calcium carbonate system. This was done by building a comprehensive model for the calcium carbonate system which consisted of nucleation, growth, aggregation, and liquid chemistry. The physics of mixing for the calcium carbonate system were also considered.

ACC is of key interest in the calcium carbonate system since it is the first solid phase to appear in the cascade of polymorphs that follow. Equilibrium concentrations of emerging ACC types were adjusted by taking into account non-idealities. The similarity between ACC and vaterite equilibrium can be seen in Figure 1.1. Kinetic effects due to operating at pseudo-steady-state were also accounted for as seen in Figure 4.3.

Legacy equilibrium expressions were shown to accurately describe the equilibrium behavior exhibited by ACC nano-particles [1,4,56]. These expressions were tested in accordance with data found in Ref. [1].

The equilibrium constant of proto-vaterite ACC and proto-calcite ACC are reported in this work to equal K_{sp}=1.80E-8 at 24 ^{o}C (Figure 4.3). The IAP equilibrium value of proto-type ACC is an order of magnitude lower than conventional ACC [2, 8, 11] and a factor of 1.45 higher than vaterite's solubility product [4]. This IAP takes into account non-idealities ignored in Ref. [1], which reported values of 3.1E-8 and 3.8E-8 mol^{-2} for the solubility product. The existence of two discrete solubility constants for these emerging ACC types was not observed in this work.

A nucleation model has been presented based on nano-particle collision mechanics. The model may be used as a replacement of classical nucleation for aqueous systems through its increased functionality and better physical representation of nucleation processes. In accordance with recent findings [19, 49, 50], the model assumes that prenucleation embryos form chains, rather than spheres, which ultimately aggregate into a nucleate as a sphere. This theory offers promising avenues in the development of crystallization theory as the model's nucleation dependency on supersaturation has similar characteristics to that of the well-studied $BaSO_4$ system [27, 48, 59, 60].

Several of the physical properties of ACC presented in the scientific literature have been presented indicating a wide variety of amorphous phases. Emphasis was placed on the physical properties (density, equilibrium constants, and water content) because of their value in precipitation models. Based on the solubilities of proto-vaterite and proto-calcite, the ACC synthesized in Ref. [1] may be characterized more effectively as disordered vaterite or vaterite with a high defect density.

Four solid-phase kinetic mechanisms were applied to a system for which kinetic data was available. Two of these models were based on classical-nucleation theory and two used the meso-crystallization models – each making different assumptions about the prenucleation distribution. Of these four models, the meso-equilibrium model and the interface-limited classical-nucleation models matched the experimental data the best. This is significant because of recent claims that this system does not follow classical-nucleation mechanisms [12]. Note, however that these model are only applicable over a very narrow concentration range.

Time-scales of the calcium carbonate system are shown to overlap mixing scales. This indicates that the rate of mixing may allow one polymorph to dominate over others by altering polymorphic preference of the system. Work should be continued to study the effects of mixing on calcium carbonate precipitation.

The results in this work indicate that calcium carbonate is not comprehensively described by classical nucleation. Several features of the system are not captured by using classical homogeneous nucleation theory, which are:

- The polymorphic preference over a broad range of conditions primarily due to the pH of the system, concentrations of the system, additive effects and temperature effects.
- Concentration dependence of the nucleation rate.
- Nucleation induction time.
- Temperature effects.

CNT is able to capture IAP traces of for a single set of conditions, however the tuned surface energies are not applicable outside of those conditions. While an extension of classical theory may be able to capture this, no work to date has done so.

6.1 Future Work

- Based on recommendations from literature sources, [1,26], it is likely that steric effects are responsible for the poor agreement between the models and nucleation theory. This is because of strong intermolecular interactions between prenucleation clusters and the aqueous phase. Consequently, use of the steric factor ΔU is advised in pursuing a comprehensive kinetic model for calcium carbonate precipitation. Note that the parameter ΔU is still used in accordance with CNT, and is a brute force approach, as it would require parameterizing ΔU in terms of additive concentration. It is possible that pH and temperature sensitivity may also need to be built into ΔU. The benefit to using ΔU is that it will correct the computation of the nucleation rate as a function of the IAP.

  In advancing the development of this parameter for the calcium carbonate system, nucleation rates could be fitted directly (rather than fitting surface energies). The new fitting parameters for nucleation would be a pre-exponential term and an exponential term. Theory describing these terms could then be investigated (i.e. temperature dependence of the pre-exponential and exponential terms). Once the functional dependence of these terms is known more elegant nucleation models could be further developed.

- Due to the complexity and lack of data nucleation rate data for calcium carbonate, meso-nucleation models should be developed in the barium sulfate system. The meso-nucleation can more readily be developed for the barium sulfate system because its nucleation rates have been experimentally measured and correlated with supersaturation ratio. There is a great deal of mystery behind what drives nucleation within the heterogeneous regime for barium sulfate, hence a study on barium sulfate would advance nucleation theory of aqueous systems in general.

- In combination with improving the equilibrium model, molecular simulations may offer insight into this complex system. The molecular simulations may increase our understanding of the steric inhibitions and precipitation mechanisms of calcium carbonate. They may also offer means to approximate ΔU, as there is no current means to measure the value.

  A software package known as Large-scale Atomic/Molecular Massively Parallel Simulator (LAMMPS) may offer means to simulate these systems. LAAMPS is an open source code which uses several different force-field models to simulate atomistic interactions. While it is primarily used to understand protein folding and polymer behavior, it can also model systems with Coulombic point-wise potentials in aqueous ionic systems.

  Using LAAMPS, work to understand the unknown transformation mechanisms of ACC into anhydrous polymorphs could also be pursued. Ref. [66] has qualitatively shown ACC transformation to have multiple pathways, but has provided no theoretical basis for the phenomena. Figure 4.4 has interesting mechanistic implications that could be explored to advance our understanding of calcium carbonate nucleation.

- Proto-type ACC should be further investigated as its solubility is suspiciously close to vaterite. This are several ways to investigated this. The experiment could be redone using in-situ x-ray diffraction, to closely monitor the formation of crystalline phases. Alternatively, the dosing of calcium ions could be halted during stage II of the experiment. Then using a chemistry model the meta-stable equilibrium point can be investigated. To improve the accuracy of this second method, a more robust chemistry model such as the Pizter formulation should be implemented.

APPENDIX A

In this Appendix, 0-D simulation results are compared to experimental data collected by Ogino et al. [2]. Many of the methods and models used in this thesis were used to generate these simulation results. The results here used the nucleation parameters found in Table A.1.

For a broad overview of the experiment conducted by Ogino et al. [2] and its importance see Chapter 1. Ogino et al. traced the ion activity product (IAP) of calcium and carbonate ions as various polymorphs precipitated. They also traced the polymorphic fraction as a function of time. Using the methods presented in this thesis, simulation results were generated based on the following operating parameters and assumptions:

- All nucleation processes are based on homogeneous classical nucleation theory, where nucleation formation is kinetically limited by interface processes (see Chapter 3).
- The energies of interface transfer values are not known, and are assumed to be constant values, discussed below.
- Growth processes are limited on both growth and interface processes (see Equation 3.40).
- The steric factor for aggregation was equal to 1E-2 for all polymorphs and ACC.
- The interfacial energies were set to optimal values in which the models performed best at 25 ^{o}C.
- The dynamics of the prenucleation distribution are taken into account using Equation 3.25. The effects of variable supersaturation were also included.
- The various polymorphic phases and ACC are assumed to not interact with each other, yet form concurrently.
- All particles are assumed to be spherical in terms of their interfacial energy and aggregation mechanics.

- The equilibrium chemistry was initialized in accordance with the concentrations used by Ogino et al. [2], these concentrations are described in Chapter 1. The amount of sodium chloride added to adjust the ionic strength was 0.1415 moles per 0.87 L of liquid.

- Instantaneous mixing is assumed, with no mass flow in or out of the system, in accordance with the setup of Ogino et al. [2].

- An adaptive explicit ODE solver was used, where the maximum time step was given by Equation 5.1 multiplied by a safety factor, in this case 2.5E-3. The simulation took about 30 minutes to finish.

- The time delay expression (Equation 3.25) was used to account for the nucleation delay (see Ref. [45, 46]).

- Ogino et al. [2] did a short mixing study where reactants were slowly mixed and results were monitored. They then executed the experiment again when quickly mixing reactants and found the results to be the same. Hence the assumption of a perfectly mixed reactor is sufficient.

The parameter ΔU, was approximated based on the general understanding of calcium carbonate and surface tension. The assumed values shown in Figure A.1 were chosen based on the experimental observation that aragonite is favored at high temperatures , calcite at low temperatures and vaterite at intermediate temperatures [2]. Secondly, aragonite forms rod shaped crystals in solution which implies that aragonite nucleation is not interfacially limited; if it were, it would be more spherical, as this reduces the interfacial area between the phases. Within the current theoretical framework, the alternative is for it to be interface controlled, which implies a high value for ΔU. Also heuristically, aqueous systems range 10-20 kcal for this parameter [45].

Table A.1: Table of values used for nucleation when simulating the system studied by Ogino et al. [2]. Here ΔU is the energy of interface transfer, σ_{bj} is the interfacial surface energy between phase j and the bulk phase, and ϕ is the steric factor for aggregation.

Parameter	ACC	vaterite	aragonite	calcite
ΔU	5.0 kcal/mol	10.0 kcal/mol	12.5 kcal/mol	10.5 kcal/mol
σ_{bj}	38.0 mJ/m^2	26.0 mJ/m^2	40.0 mJ/m^2	112.8 mJ/m^2
ϕ_j	1E-2	1E-6	1E-6	1E-6

The interfacial tension, σ_{bj}, was tuned to fit the data directly, based on the above assumptions for ΔU. The values of ϕ were also approximated based on heuristics from Stumm and Morgan [33] (see Chapter 3 for details).

Figures A.1 and A.2 show the temporal IAP trace of the experimental data and the simulated results, both at 25^oC. Note that the cascade in the IAP throughout the experiment due to different solid phases precipitating and dissolving. The inflection point, denoted by the symbol a, was experimentally found to be reproducible, but was not reproduced using this model. Many of the features of this curve are captured by the model, including the initial drop off time, and the time that it takes to reach calcite equilibrium.

Experimental data for the solid phase dynamics can be found in Figure A.3. This data agrees well with simulation results shown in Figure A.4. Between these two figures, two key features are in agreement, including the delayed formation of vaterite, vaterite and calcite being equally favored at the 5 minute point in the experiment. Note that the data presented in Figures A.1 and A.3 come directly from Ogino et al. [2] and has not been not corrected using Equation 1.2.

Simulations show poor agreement with data outside of 25^oC and at compositional space beyond what has been investigated in the short case study presented in this appendix. This is primarily due to the great deal uncertainty of kinetic constants available and lack of development of models for calcium carbonate precipitation. Regardless of uncertainty, the current model can be improved. Different values of ΔU should be explored as this study used

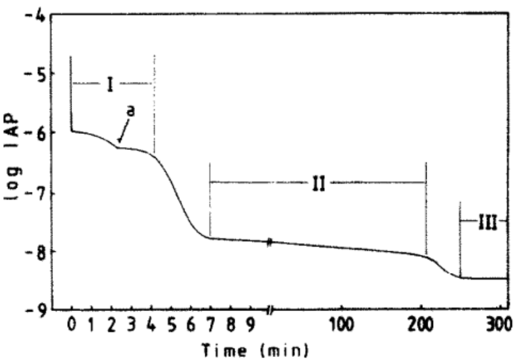

Figure A.1: Figure taken from Ref. [2]. Experimental data from work done by Ogino et al. [2] at 25^{o}C; the IAP trace of the experiment. The feature denoted with the symbol a is named the inflection point.

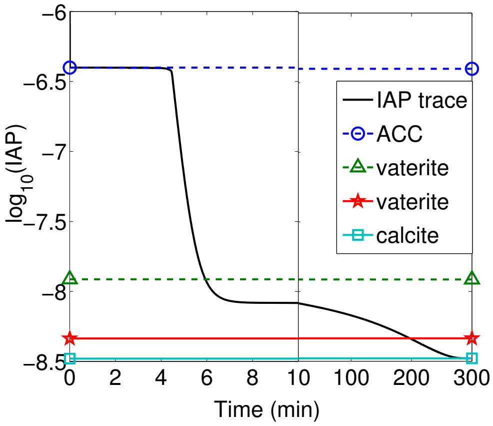

Figure A.2: 0-D IAP simulation results at 25^{o}C of the experiment by Ogino et al. [2]; the IAP trace of the experiment.

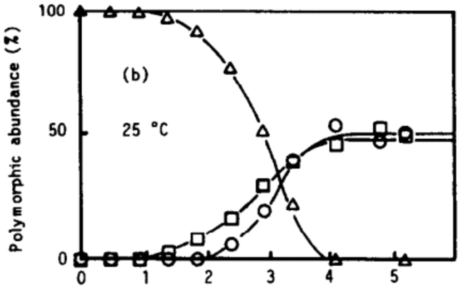

Figure A.3: Figure taken from Ref. [2]. Experimental data from work done by Ogino et al. [2] at 25^{o}C; the polymorphic selectivity trace of the experiment. The symbols are defined as follows: ○-ACC, △-vaterite, □-calcite

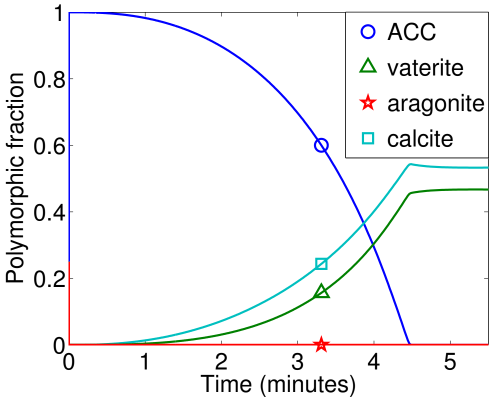

Figure A.4: Simulation results of the Ogino et al. [2] system, showing the polymorphic selectivity of calcium carbonate precipitation at 25^o as a function of time

values are based off heuristics and intuition. The activity coefficients can have temperature dependence built into them to match the data with greater accuracy (an approach taken in Appendix B.)

APPENDIX B

In this appendix, 1-D simulation results of calcium carbonate nucleation are presented. The simulations used the ODT model running at operating conditions on systems from an industrial collaborator. The results in this appendix are based on concentrations where no experimental data are available.

The kinetic models used in ODT are based on kinetic mechanisms developed in this thesis, however, slight variations were made to the models. These can be found in detail in Ref. [3]. A brief summary of these differences is that nucleation includes an additional parameter known as the Tollman length [47], and an aggregation model based on experimental data [55]. Surface energies are assumed to be linearly dependent upon temperature given by

$$\sigma_{bj} = \sigma_{bj,0} + S_{ae}(T - T_0). \tag{B.1}$$

Here, $\sigma_{bj,0}$ is the interfacial surface energy at temperature T_0, S_{ae} is the linear dependence of the surface energy. A set of eight parameters (two for each polymorph) were fitted to data from Ogino et al. using the simplex method, a technique for numerical optimization [3]. The optimized parameters are given in table B.2.

The fitted parameters are limited to a narrow range of operating conditions, similar to the problem with the approach taken in Appendix A. However, these parameters capture temperature effects well for the experiments in Ref. [2]. These parameters were coded into ODT so that the effects of mixing could be investigated.

Table B.2: Table of nucleation parameters used in ODT, generated from optimizing models with data. The temperature dependence of parameters based on 25 ^{o}C.

Parameter	ACC	vaterite	aragonite	calcite
$\sigma_{bj,0}$	56.0 mJ/m^2	148 mJ/m^2	185 mJ/m^2	176 mJ/m^2
S_{ae}	9.09E-5 mJ/m^2/K	8.67E-5 mJ/m^2/K	-2.18e-4 mJ/m^2/K	6.42E-5 mJ/m^2/K

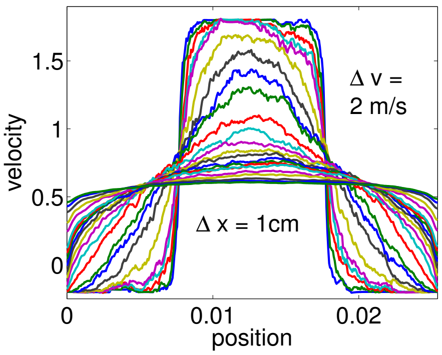

Figure B.1: Plot of the mean velocity (in meters per second) as a function of location (in meters) in a periodic jet. Times range from zero to one second.

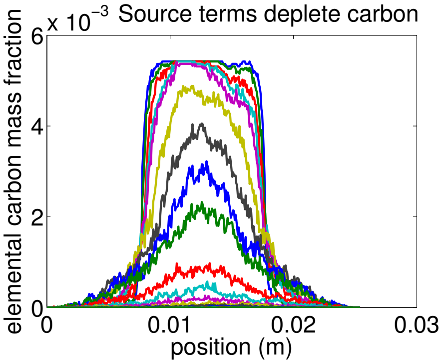

Figure B.2: Shows the evolution of the carbon mass (dimensionless) fraction of ODT, in a periodic jet as a function of location (in meters). Times range from zero to one second.

Once these parameters and their respective models were coded into ODT, simulations were generated to show turbulence and kinetic modeling integration. However, since the above-mentioned kinetic model is only valid over a very narrow of operating conditions, these results are thought to be unphysical. This is because for systems of similar, high concentrations, ACC remains the dominant solid phase for much longer than one second [67]. Hence the the kinetic model over-predicts nucleation rates and or dissolution rates at high supersaturation ratios, and under-predicts nucleation rates at low supersaturation ratios. Regardless, ODT results are presented here as a proof of concept.

On a Linux supercomputing cluster, ODT ran on one-hundred simulations in which flow statistics were generated. The results shown here are generated from the statistical average of these one-hundred realizations. The flow configuration had 0.55 molar $NaCO_3$ flowing out of a orifice into a solution of 0.62 molar $CaCl_2$. The jet is periodic and hence is *not a true jet* since the surrounding fluid is not infinite. This was done to preserve the stoichiometric ratio of the two streams. Figure B.1 shows the velocity profile of a periodic temporal jet at times, which range from zero to one second. The operating parameters for the flow configuration are given in Table B.3.

Table B.3: Table of flow parameters used for the temporal periodic jet in ODT.

Jet velocity, v_0	Viscosity, μ	Jet diameter, D_J	Fluid density, ρ
2.0 m/s	8.91E-4 kg/m/s^2	1.0E-2 m	1000 kg/m^3

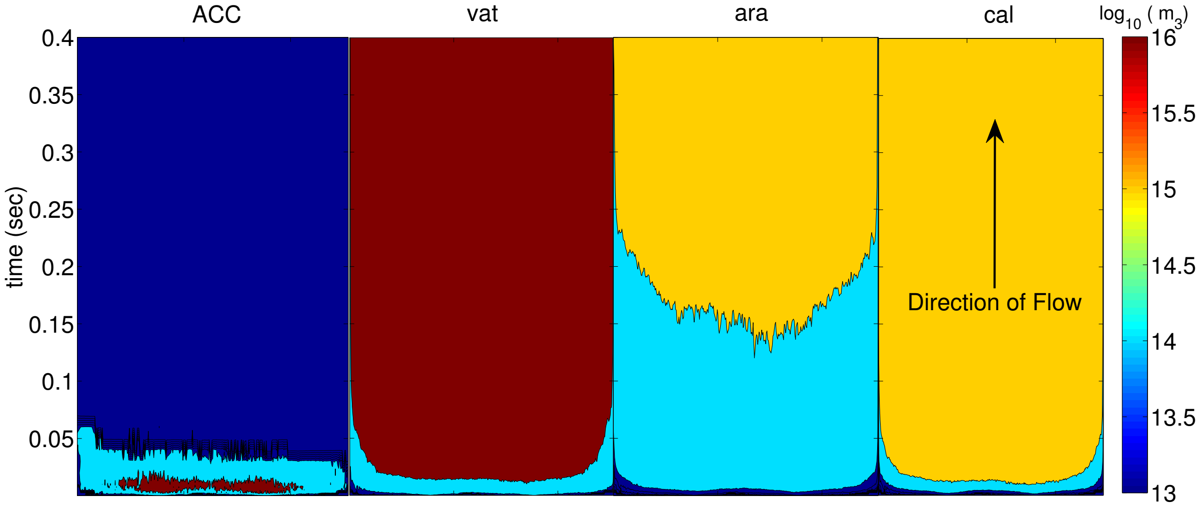

Figure B.3: Shows the mean spatial values of the third moment for each of the polymorphs. The third moment has units of μm^3/m^3.

Figure B.2 shows the mass fraction of carbon decreases due to precipitation. At the end of the simulation, carbon is in equilibrium with meta-stable vaterite. The particles that consequently form are represented by moments. The third moment of the distribution is directly proportional to the total volume of particles in solution. Four sets of third moments are generated, one for each polymorph, in this case, calcite, aragonite, vaterite, and ACC. These moments can be seen in Figure B.3. The units are μm^3/m^3, meaning that roughly 1% of the fluid flow is particles. When values along the x-axis of Figure B.3 are averaged, Figure B.4 results. This shows that the kinetics predicted are much faster than similar systems even. When Figure B.4 is compared to data from [67], who performed a ACC precipitation experiment using 1.0 molar solutions in a beaker, it shows that ACC forms and dissolves much faster than found experimentally.

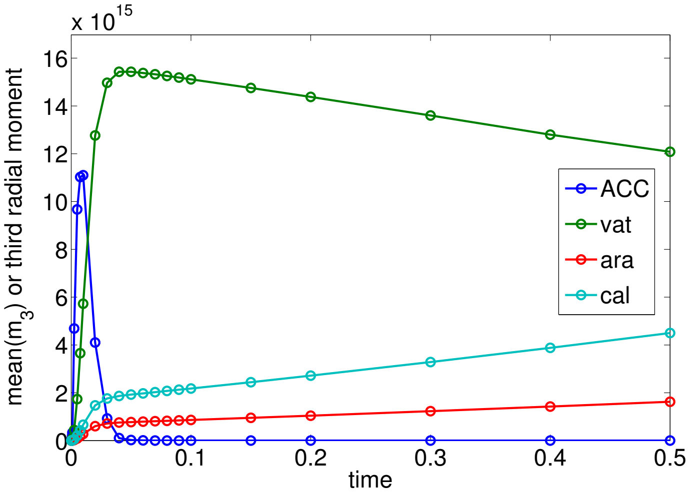

Figure B.4: Shows the mean spatially-averaged values of the third moments for each of the polymorphs. The third moment has units of $\mu m^3/m^3$. ACC precipitates in less than 50 ms, contrary to what is seen experimentally [67].

The kinetics were shown to not be important for polymorph selectivity using this kinetic model. When the kinetics from the 0-D models are compared to results using ODT there is a significant change in the overall time scales of the system. However, there is no change in the polymorphic selectivity of the system. Rather, the kinetics are limited by mixing, and form the same dominant polymorphs based on the chemical system the kinetics were tuned to match.

REFERENCES

[1] D. Gebauer, A. Volkel, and H. Colfen. Stable prenucleation calcium carbonate clusters. *Science*, 322:1819–1822, 2008.

[2] T. Ogino, T. Suzuki, and K. Sawada. The formation and transformation mechanism of calcium carbonate in water. *Geochim. Cosmochim. Ac.*, 51:2757–2767, 1987.

[3] B. B. Schroeder, D. D. Harris, S. T. Smith, and D. O. Lignell. A theoretical framework for calcium-carbonate precipitation with multiple polymorphs, May 2013. submitted to Geochimica et Cosmochimica Acta.

[4] L. Plummer and E. Busenberg. The solubilities of calcite, aragonite and vaterite in CO_2-H_2O solutions between 0 and 90 ^oC, and an evaluation of the aqueous model for the system $CaCO_3$-CO_2-H_2O. *Geochim. Cosmochim. Ac.*, 46:1011–1040, 1982.

[5] D. Kralj and L. Brecevic. Dissolution kientics and solubilities of calcium carbonate monohydrate. *Colloid Surface A.*, 96:287–293, 1995.

[6] A. Radha, T. Forbes, C. Killian, P. Gilbert, and A. Navrotsky. Transformation and crystallization of energetics of synthetic and biogenic amorhpous calcium carbonate. *Proc. Natl. Acad. Sci.*, 107:16438–16443, 2010.

[7] J. Cartwright, A. Checa, J. Gale, D. Gebauer, and C. Sainz-Diaz. Calcium carbonate polymorphism and its role in biomineralization: how many amorphous calcium carbonates are there? *Angew. Chem. Int. Ed.*, 51:11960–11970, 2012.

[8] L. Brecevic and A. Nielsen. Solubility of amorphous calcium carbonate. *J. Cryst. Growth*, 98:504–511, 1989.

[9] J. Bolze, B. Peng, N. Dingenouts, P. Panine, T. Narayanan, and M. Ballauff. Formation and growth of amorphous colloidal $CaCO_3$ precurser particles as detected by time-resolved SAXS. *Langmuir*, 18:8364–8369, 2002.

[10] J. Bolze, D. Pontoni, M. Ballauff, T. Narayanan, and H. Colfen. Time-resolved SAXS study of the effect of a double hydrophilic block-copolymer on the formation of $CaCO_3$ from a supersaturated salt solution. *J. Colloid. Interf. Sci.*, 277:84–94, 2004.

[11] J. Clarkson, T. Price, and C. Adams. Role of metastable phases in the spontaneous precipitation of calcium carbonate. *J. Chem. Soc. Faraday Trans.*, 88:243–249, 1992.

[12] D. Gebauer and H. Colfen. Prenucleation clusters and non-classical nucleation. *Nano Today*, 6:564–584, 2011.

[13] A. Goodwin, F. Michel, B. Phillips, D. Keen, M. Dove, and R. Reeder. Nanoporous structure and medium-range order in synthetics amorphous calcium carbonate. *Chem. Mater.*, 22:3197–3205, 2010.

[14] F. Michel, J. MacDonald, J. Feng, B. Phillips, L. Ehm, C. Tarabrella, J. Parise, and R. Reeder. Structural characteristics of synthetic amorphous calcium carbonate. *Chem. Mater.*, 20:4720–4728, 2008.

[15] Y. Han, G. Hadiko, M. Fugi, and M. Takahashi. Factors affecting the phase and morphology of $CaCO_3$ prepared by a bubbling method. *J. Eur. Ceram. Soc.*, 26:843–847, 2006.

[16] H. Nebel, M. Neumann, C. Mayer, and M. Epple. On the structure of amorphous calcium carbonate - a detailed study by solid-state nmr spectroscopy. *Inorg. Chem.*, 47:7874–7879, 2008.

[17] S. Wolf, J. Leiterer, V. Pipich, R. Barrea, F. Emmerling, and W. Tremel. Strong stabilization of amorphous calcium carbonate emulsion by ovalbumin: gaining insight into the mechanism of polymer-induced liquid precurser processes. *J. Am. Chem. Soc.*, 133:12642–12649, 2011.

[18] D. Gebauer, P. Gunawidjaja, J. Ko, Z. Bacsik, B. Aziz, L. Liu, Y. Hu, L. Bergstrom, C. Tai, T. Sham, M. Eden, and N. Hedin. Proto-calcite and proto-vaterite in amorphous calcium carbonates. *Angew. Chem. Int. Ed.*, 49:8889–8891, 2010.

[19] R. Demichelis, P Raiteri, J. Gale, D. Quigley, and D. Gebauer. Stable prenucleation mineral clusters are liquid-like ionic polymers. *Nat. Commun.*, 2:590, 2011.

[20] R. Sear. The non-classical nucleation of crystals: microscopic mechanisms and applications to molecular crystals, ice and calcium carbonate. *Int. Mat. Rev.*, 57:328–356, 2012.

[21] I. Duedall and D. Buckley. Calcium carbonate monohydrate in seawater. *Nature Phys. Sci.*, 234:39–40, 1971.

[22] R. van Tassel. Carbonate precipitation of mixed calcium-magnesium chloride solutions. *Z. Anorg. Allg. Chem.*, 319:107, 1962.

[23] J. Bischoff, J. Fitzpatrick, and R. Rosenbauer. The solubility and stabilization of ikaite. *J. Geol.*, 101:21–33, 1993.

[24] M. Faatz, W. Cheng, and G. Wegner. Mechanical strength of amorphous $CaCO_3$ colloidal spheres. *Langmuir*, 21:6666–6668, 2005.

[25] M. Saharay, A. Yazaydin, and R. Kirkpatrick. Dehydration-induced amorphous phases of calcium carbonate. *J. Phys. Chem.*, 117:3328–3336, 2013.

[26] P. Raiteri and J. D. Gale. Water is the key to nonclassical nucleation of amorphous calcium carbonate. *J. Am. Chem.*, 132:17623–17634, 2010.

[27] D. Kashchiev and G. van Rosmalen. Review: Nucleation in solutions revisited. *Cryst. Res. Technol.*, 38:555–574, 2003.

[28] A. Mersmann. Calculation of interfacial tensions. *J. Cryst. Growth*, 1990:841–847, 102.

[29] V. LaMer and R. Dinegar. Theory, production and mechanism of formation of monodispersed hydrosols. *Journal of the american chemical society*, 72:4847–4854, 1950.

[30] D. Kralj, L. Brecevic, and J. Kontrec. Vaterite growth and dissolution in aqueous solution III. kinetics of transformation. *J. Cryst. Growth*, 177:248–257, 1997.

[31] N. Abdel-Aal and K. Sawada. Inhibition of adhesion and precipitation of $CaCO_3$ by aminopolyphosphonate. *J. Cryst. Growth*, 256:188–200, 2003.

[32] T. Ogino, T. Suzuki, and K. Sawada. The rate and mechanism of polymorphic transformation of calcium carbonate. *J. Cryst. Growth*, 100:159–167, 1990.

[33] W. Stumm and J. J. Morgan. *Aquatic Chemistry.* John Wiley and Sons Inc., third edition, 1996.

[34] H. Frank and P. Thompson. Fluctuations and the limited of validty of the debye-huckel theory. *J. Chem. Phys.*, 1959:1086–1096, 31.

[35] J. Mayer. The theory of ionic solutions. *J. Chem. Phys.*, 18:1426–1436, 1950.

[36] O. Redlich. The dissociation of strong electrolytes. *Chem. Rev.*, 39:333–356, 1946.

[37] R. Fox. Optimal moment sets for multivariate direct quadrature method of moments. *Ind. Eng. Chem. Res.*, 48:9686–9696, 2009.

[38] A. D. Randolph and M. A. Larson. *Theory of particulate processes.* Academic Press, 1988.

[39] R. McGraw. Description of aerosol dynamics by the quadrature method of moments. *Aerosol Science and Technology*, 25:255–265, 1997.

[40] A. R. Kerstein. One-dimensional turbulence: model formulation and application to homogeneous turbulence, shear flows, and buoyant stratified flows. *Journal of Fluid Mechanics*, 392:277–334, 1999.

[41] D. O. Lignell, A. R. Kerstein, G. Sun, and E. I. Monson. Mesh adaption for efficient multiscale implementation of one-dimensional turbulence. *Theor. Comput. Fluid Dyn.*, 27:273–295, 2012.

[42] J. Kawano, N. Shimobayashi, A. Miyake, and M. Kitamura. Precipitation diagram of calcium carbonate polymorphs: its construction and significance. *J. Phys.: Condens. Matter*, 21:1–6, 2009.

[43] S. Rigopoulos and A. Jones. Modeling of semibatch agglomerative gas-liquid precipitation of $CaCO_3$ in a bubble column reactor. *Ind. Eng. Chem. Res.*, 42:6567–6575, 2003.

[44] P. Chiang, M. Donohue, and J. Katz. A kinetic approach to crystallization from ionic solution. *J. Colloid. Interf. Sci.*, 122:251–265, 1988.

[45] Ivan Markov. *Crystal growth for beginners: fundamentals of nucleation, crystal growth, and epitaxy.* World Scientific, 1995.

[46] D. Kashchiev. *Nucleation.* Butterworth-Heinemann, 2000.

[47] Richard C. Tolman. The effect of droplet size on surface tension. *J. Chem. Phys.*, 17:333–337, 1949.

[48] H. Schubert and A. Mersmann. Determination of heterogeneous nucleation rates. *Trans. IChemE.*, 74:821–827, 1996.

[49] D. Erdemir, A. Lee, and A. Myerson. Nucleation of crystals from solution: classical and two-step models. *Accounts Chem. Res.*, 42:621–629, 2009.

[50] P. Wolde, D. Oxtoby, and D. Frenkel. Chain formation in homogeneous gas-liquid nucleation of polar fluids. *J. Chem. Phys.*, 111:4762–4773, 1999.

[51] H. Colfen and M. Antonietti. *Mesocrystals and Nonclassical Crystallization.* Wiley, 2008.

[52] J. Moore and R. Pearson. *Kinetics and Mechanism.* Wiley-Interscience, 1981.

[53] J. A. Dirksen and T. A. Ring. Fundamentals of crystallization: Kinetic effects on particle size distribution and morphology. *Chem. Eng. Sci.*, 46:2389–2427, 1991.

[54] D. L. Marchisio, J. T. Pikturna, R. O. Fox, R. D. Vigil, and A. A. Barresi. Quadrature method of moments for population-balance equations. *AIChE Journal*, 49:1266–1276, 2003.

[55] T. L. Liew, J. P. Barrick, and M.J Hounslow. A micro-mechanical model for the rate of aggregation. *Chem. Eng. Tech.*, 3:282–285, 2003.

[56] G. Nancollas. *Interaction in electroylyte solutions (metal complex and ion-pair formation in solution).* Elsevier, 1966.

[57] M. Wolf, O. Breitkopf, and R. Puk. Solubility of calcite in different electrolytes at temperatures between 10^o and 60^oC and at CO_2 partial pressures of about 1kPa. *Chem. Geol.*, 76:291–301, 1989.

[58] R. Beck, M. Seiersten, and J.-P. Andreassen. The constant composition method for crystallization of calcium carbonate at constant supersaturation. *J. Cryst. Growth*, 380:187–196, 2013.

[59] A. Nielsen. Homogeneous nucleation in barium sulfate precipiation. *Acta Chem. Scand.*, 15:441–442, 1961.

[60] L. Vicum, M. Mazzotti, and J. Baldyga. Applying a thermodynamic model to the non-stoichiometric precipitation of barium sulfate. *Chem. Eng. Technol.*, 26:325–333, 2003.

[61] E. Pouget, P. Bomans, J. Goos, P. Frederik, G. With, and N. Sommerdijk. The initial stages of template-controlled $CaCO_3$ formation revealed by cryo-TEM. *Science*, 323:1455–1458, 2009.

[62] D. Quigley, C. Freeman, J. Harding, and P. Rodger. Sampling the structure of calcium carbonate nanoparticles with metadynamics. *J. Chem. Phys.*, 134:044703, 2011.

[63] G. Tribello, F. Bruneval, C. Liew, and M. Parrinello. A moleculare dynamics study of the early stages of calcium carbonate growth. *J. Phys. Chem. B*, 113:11680–11687, 2009.

[64] R. Kalaba, K. Spingarn, and L. Testfatsion. Individual tracking of an eigenvalue and eigenvector of a parameterized matrix. *Nonlinear Anal-Theor*, 5:337–340, 1980.

[65] S. B. Pope. *Turbulent Flows.* Cambridge University Press, New York, 2000.

[66] P. Bots, L. Benning, J. Rodriguez-Blanco, T. Roncal-Herrero, and S. Shaw. Mechanistic insights into the crystallization of amorphous calcium carbonate. *Cryst. Growth Des.*, 12:3806–3814, 2012.

[67] J. Rodriguez-Blanco, S. Shaw, and L. G. Benning. The kinetics and mechanisms of amorphous calcium carbonate crystallization to calcite, via vaterite. *Nanoscale*, 3:265, 2011.